Insights into formation scenarios of massive early-type galaxies from spatially resolved stellar population analysis in CALIFA

Stefano Zibetti [1]★ Anna R. Gallazzi [1] Michaela Hirschmann,[2,3] Guido Consolandi,[4] Jesús Falcón-Barroso,[5,6] Glenn van de Ven [7] and Mariya Lyubenova [8]

[1]*INAF-Osservatorio Astrofisico di Arcetri, Largo Enrico Fermi 5, I-50125 Firenze, Italy*
[2]*Institut d'Astrophysique de Paris, CNRS, Université Pierre & Marie Curie, 98 bis Boulevard Arago, F-75014 Paris, France*
[3]*DARK, Niels Bohr Institute, University of Copenhagen, Lyngbyvej 2, DK-2100 Copenhagen, Denmark*
[4]*INAF-Osservatorio Astronomico di Brera, Via Brera 28, I-20121 Milano, Italy*
[5]*Instituto de Astrofísica de Canarias, Vía Láctea s/n, E-38205 La Laguna, Tenerife, Spain*
[6]*Departamento de Astrofísica, Universidad de La Laguna, E-38205 La Laguna, Tenerife, Spain*
[7]*Department of Astrophysics, University of Vienna, Türkenschanzstrasse 17, A-1180 Vienna, Austria*
[8]*European Southern Observatory, Karl-Schwarzschild-Straße 2, D-85748 Garching bei München, Germany*

ABSTRACT

We perform spatially resolved stellar population analysis for a sample of 69 early-type galaxies (ETGs) from the CALIFA integral field spectroscopic survey, including 48 ellipticals and 21 S0's. We generate and quantitatively characterize profiles of light-weighted mean stellar age and metallicity within $\lesssim 2R_{\rm e}$, as a function of radius and stellar-mass surface density μ_*. We study in detail the dependence of profiles on galaxies' global properties, including velocity dispersion $\sigma_{\rm e}$, stellar mass, morphology. ETGs are universally characterized by strong, negative metallicity gradients (~ -0.3 dex per $R_{\rm e}$) within $1R_{\rm e}$, which flatten out moving towards larger radii. A quasi-universal local μ_*–metallicity relation emerges, which displays a residual systematic dependence on $\sigma_{\rm e}$, whereby higher $\sigma_{\rm e}$ implies higher metallicity at fixed μ_*. Age profiles are typically U-shaped, with minimum around $0.4\,R_{\rm e}$, asymptotic increase to maximum ages beyond $\sim 1.5\,R_{\rm e}$, and an increase towards the centre. The depth of the minimum and the central increase anticorrelate with $\sigma_{\rm e}$. A possible qualitative interpretation of these observations is a two-phase scenario. In the first phase, dissipative collapse occurs in the inner $1R_{\rm e}$, establishing a negative metallicity gradient. The competition between the outside-in quenching due to feedback-driven winds and some form of inside-out quenching, possibly caused by central AGN feedback or dynamical heating, determines the U-shaped age profiles. In the second phase, the accretion of ex-situ stars from quenched and low-metallicity satellites shapes the flatter stellar population profiles in the outer regions.

Key words: techniques: imaging spectroscopy – galaxies: abundances – galaxies: elliptical and lenticular, cD – galaxies: evolution – galaxies:formation – galaxies: stellar content.

1 INTRODUCTION

Massive early-type galaxies (ETGs, hereafter) have been a critical benchmark for models of galaxy formation and evolution since several decades. The vast majority of these galaxies have been almost completely depleted of cold interstellar medium (ISM) and lacking substantial star-formation activity for several Gyr. The degree of metal enrichment in their stars, typically at supersolar level, implies that, relative to the general galaxy population, massive

ETGs have been able to reprocess their ISM more efficiently, with fewer losses of metals and in shorter times, as suggested by their relative enhanced ratio of α elements with respect to iron. On the one hand, their global properties appeared similar to the natural outcome of a dissipative collapse regulated by stellar feedback (historically dubbed as 'monolithic' collapse scenario, e.g. Eggen, Lynden-Bell & Sandage 1962; Larson 1974) and, on the other hand, their scaling relations are not immediately reconcilable with naïve expectations from Cold Dark Matter (CDM) hierarchical models (e.g. Renzini 2006, and reference therein). According to these expectations, massive ETGs, as the most massive galaxies in the present-day Universe, should 'form' later than less massive galaxies (including

★ E-mail: stefano.zibetti@inaf.it

late types), but the analysis of their stellar content clearly indicates that most of their stars formed early on and little new stars were added in the last 5–8 Gyr, as opposed to less massive galaxies, which contain much younger stars or are even still currently forming stars. This challenge to hierarchical models, often referred to as the 'anti-hierarchical nature of ETGs', was mostly settled in the second half of the years 2000's by a number of theoretical works (most notably De Lucia et al. 2006; Neistein, van den Bosch & Dekel 2006). They pointed out the fundamental difference between the halo assembly history and the star formation history integrated over all progenitors. They showed that while the former is obviously hierarchical in CDM models, so that more massive haloes are formed later via merging of less massive ones, the integrated star formation history of the progenitors is actually shifted back in time for more massive haloes as a natural consequence of their progenitor haloes forming earlier in higher density peaks (Neistein et al. 2006).

At the same time as the hierarchical-monolithic debate was having its acme, semi-analytic models (SAMs) of galaxy formation and evolution based on CDM N-body cosmological simulations had to face another major problem in the formation of massive ETGs. It was found that no thermodynamical or stellar feedback mechanism is able to stop gas from being accreted on to massive haloes/galaxies from the cosmic network, cooling down and forming stars. Radiative and mechanical feedback from the active galactic nuclei (AGNs), powered by the supermassive black hole lurking in galaxy centres, was then identified as responsible for the 'quenching' and the inhibition of star formation in massive ETGs (e.g. Croton et al. 2006). Later on, it was realized that the development of a massive/dense stellar spheroid can also stabilize the gas and prevent its transformation into stars, thus giving rise to the so-called morphological quenching mechanism (e.g. Martig et al. 2009), which represents a possible alternative for AGN feedback, especially for galaxies less massive than $M_{halo} \sim 10^{12}\,M_\odot$. So far, a detailed description of when, where, and how these mechanisms are at work still defies our theoretical understanding and observational tests.

In fact, we still lack a fully consistent theoretical framework that is able to account for several other crucial (sets of) observations: (i) the evolution of the mass–size relation across cosmic times, whereby ETGs at fixed stellar mass are on average a factor ~ 4 more extended now than at redshift $\gtrsim 2$ (e.g. van der Wel et al. 2014); (ii) the different properties of slow and fast rotators (e.g. Emsellem et al. 2011); (iii) the internal structure and the variation of stellar populations across the spatial extent of the ETGs, which are the focus of this paper; (iv) the enhancement of α elements with respect to iron and its relation to total stellar mass or velocity dispersion (e.g. Trager et al. 2000; Gallazzi et al. 2006); (v) the alleged variation of stellar initial mass function (IMF), with bottom-heavier IMF being predominant in more massive ETGs and in the cores/densest regions (e.g. Conroy & van Dokkum 2012; Ferreras et al. 2013; Martín-Navarro et al. 2015).

It is arguable that these phenomena should essentially result from the interplay of the basic mechanisms we highlighted in this introduction: the dissipative collapse of gas and the stellar feedback; the mergers, either as major mergers of similar-mass progenitors or as minor mergers, i.e. accretion of satellites; the feedback from the AGN; the morphological quenching that follows the formation of a massive and dense stellar spheroid. When, where, and how these mechanisms take place determines spatial and temporal variations in the physical conditions in which stars are formed and in the dynamics of the stars that are formed and/or accreted. The archaeological memory of these processes is retained in the stellar population properties of present-day massive ETGs.

Their spatial variations, in particular, can help unravel the complex interplay of different mechanisms.

From a theoretical perspective, starting with the seminal work by De Lucia et al. (2006), a two phase scenario for the formation of ETGs (and elliptical galaxies in particular) has increasingly gained support both from semi-analytic models and from cosmological simulations. Quoting from Oser et al. (2010), who ran a set of cosmological simulations and were the first to explicitly propose a 'two-phase scenario', the formation of ETGs would consist of 'a rapid early phase at $z \gtrsim 2$ during which '*in situ*' stars are formed within the galaxy from infalling cold gas followed by an extended phase since $z \lesssim 3$ during which 'ex situ' stars are primarily accreted'. As we will show in this paper, spatial variations of stellar population properties can actually test and prove this scenario.

From the observational point of view, although variations of stellar populations in ETGs are evident already from colour gradients (e.g. de Vaucouleurs 1961), this kind of investigation requires spatially resolved spectroscopy at moderate resolution, in order to track the spatial variation of age- and metallicity-sensitive absorption features across the galaxies. Early works relied on long-slit spectroscopy to trace absorption-feature strength variations along a radial direction (e.g. Carollo, Danziger & Buson 1993; Mehlert et al. 2003; Sánchez-Blázquez et al. 2007), and concluded that the absorption-strength gradients are essentially due to metallicity and that the age of the populations is generally more homogeneous. The advent of integral field spectroscopy (IFS) has opened a new era in this field, by empowering truly 2D-mapping capabilities in terms of stellar population properties. A number of works on the radial variations of stellar population properties in ETGs have been published in the last decade from IFS surveys (see Section 8), such as: SAURON (de Zeeuw et al. 2002), ATLAS^{3D} (Cappellari et al. 2011), SDSS-IV MaNGA (Bundy et al. 2015), SAMI (Bryant et al. 2015), and CALIFA (Sánchez et al. 2012). Despite the wealth of measurements and the improved precision of the available spectrophotometric data sets, a general *quantitative* consensus on the spatial distribution of the stellar population properties (age and metallicity, in particular) of ETGs is still lacking. Significant systematic offsets persist among different estimates, in different data sets and/or obtained with different approaches, as it will be illustrated and discussed in Section 8.

As we describe in detail in Section 3, in this paper we aim at further improving these measurements and reduce systematic uncertainties. To this goal, we adopt a Bayesian method that takes into account the most robust constraints from both spectroscopy and broadband photometry (see also Gallazzi et al. 2005; Zibetti et al. 2017). The inference of the stellar population properties is then based on a vast suite of models that aims at covering the full possible complexity in terms of star formation and chemical enrichment histories, as well as of dust attenuation, in order to fully account for degeneracies in physical parameter space at given observational constraints.

With our spatially resolved analysis we also aim at investigating the role of different scales in shaping the (spatial distribution of the) stellar population properties of ETGs, in a sort of closer examination of the questions already addressed in our previous work (Zibetti et al. 2017): (i) Is it *local* (~ 1 kpc) scales what determines the local stellar population properties (e.g. González Delgado et al. 2014, 2016; Barrera-Ballesteros et al. 2016; Cano-Díaz et al. 2016)? (ii) Or is it a global parameter, such as mass (e.g. Gavazzi & Scodeggio 1996; Scodeggio et al. 2002; Kauffmann et al. 2003), velocity dispersion (e.g. Bender, Burstein & Faber 1993; Gallazzi et al. 2006), or overall age, what local properties mostly respond to?

The paper is organized as follows. Section 2 introduces the sample of ETGs and the data set used for the analysis. Section 3 provides full details on the methods and the data processing used to infer 2D maps of the stellar population ages and metallicities. Section 4 describes individual profiles of age and metallicity as a function of radius and of surface brightness/mass density. Methods of extraction and uncertainties are presented and discussed, as well as general trends. Section 5 analyses the average stellar population profiles for galaxies binned in classes of different global properties, such as mass, velocity dispersion, and E/S0 morphology. The dependence of the stellar population profiles on global properties is quantified in Section 6. In Section 7 we focus on the descriptions of the profiles in terms of gradients, as a convenient and popular way of compressing the information about the shape of the profiles. Correlations and trends with global quantities are also analysed. In Section 8 we discuss our results in the context of the vast literature on the topic and propose a physical interpretation of our findings. Section 9 summarizes and concludes this paper.

## 2 THE CALIFA-SDSS ETG SAMPLE AND DATA SET

This study is based on a sample of ETGs drawn from the main diameter-selected sample of the Calar Alto Legacy Integral Field Area (CALIFA) survey (Sánchez et al. 2012; Walcher et al. 2014) in its third and final data release (Sánchez et al. 2016, DR3). Apart from celestial coordinate constraints, these galaxies are selected from the seventh data release of the Sloan Digital Sky Survey (Abazajian et al. 2009) requiring isophotal r-band diameter 45 arcsec $< isoA_r <$ 79.2 arcsec, r-band Petrosian magnitude <20 and available redshift $0.005 < z < 0.03$ (see Walcher et al. 2014).

Galaxies are observed in integral-field spectroscopy at the 3.5 m telescope of the Calar Alto observatory with the Potsdam Multi-Aperture Spectrograph, PMAS (Roth et al. 2005) in the PPAK mode (Verheijen et al. 2004; Kelz et al. 2006). The hexagonal field of view of 74 arcsec × 64 arcsec is covered by a bundle of 331 science fibres, in three dithers that provide an effective filling factor close to 100 per cent. Out of the 542 observed main sample galaxies, we consider only the 394 galaxies that have been observed in both the blue 'V1200' and red 'V500' setups, combined into the so-called COMBO data cubes[1] The unvignetted spectral coverage extends from 3700 to 7140 Å, with a spatial sampling of 1 arcsec per spaxel (effective spatial resolution ∼2.57 arcsec FWHM). These data cubes typically reach a signal-to-noise ratio (SNR) of 3 per spectral resolution element and per spaxel at ∼23.4 mag arcsec^{-2} (r-band, see fig. 14 of Sánchez et al. 2016).

From this sample we select morphologically classified ETGs, i.e. galaxies with morphological type earlier than S0a (S0a excluded), not classified as mergers (see Walcher et al. 2014). After visual inspection we further discard three galaxies that are misclassified later types than E or S0: NGC 693 (S0/a in de Vaucouleurs et al. 1991, RC3, with evident nuclear starburst), IC 3598 (SA(r)ab in RC3), and UGC 9629 (Sa in RC3). These leaves us with a sample of 69 ETGs in total, including 48 E's and 21 S0's.

Total stellar masses for each galaxy are taken from Walcher et al. (2014). We adopt the estimates based on the fitting of the

---

[1]As in Z17, we exclude UGC 11694 because of a very bright star near the centre, which contaminates a significant portion of the galaxy's optical extent, and UGC 01123 because of problems in the noise spectra.
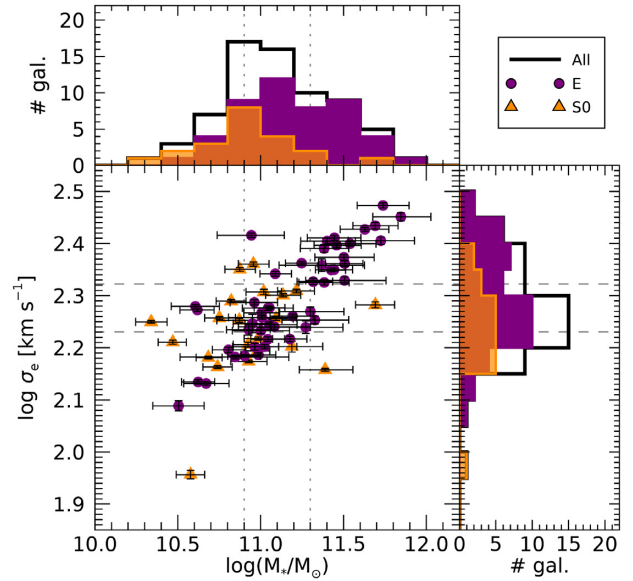
Figure 1. Distribution in M_* and velocity dispersion σ_e within $1R_e$ for the full ETG sample, and for the subsamples of ellipticals and S0, in purple and dark orange, respectively. The vertical dotted lines (at $M_*/M_\odot = 10^{10.9} = 7.9 \times 10^{10}$ and $M_*/M_\odot = 10^{11.3} = 2 \times 10^{11}$) and horizontal dashed lines (at $\sigma_e/\mathrm{km\,s^{-1}} = 170 = 10^{2.23}$ and $\sigma_e/\mathrm{km\,s^{-1}} = 210 = 10^{2.32}$) indicate the boundaries that define the three bins in stellar mass and velocity dispersion, respectively, used in the analysis.

SDSS petrosian magnitudes only, excluding UV or NIR data. We recall here that these estimates are based on the revised version of the Bruzual & Charlot (2003, BC03) stellar population synthesis models indicated in the literature as CB07, assuming a Chabrier (2003) stellar initial mass function. Note that CB07 underestimates stellar masses by ≈ 0.1 dex with respect to 'standard' BC03 models (see e.g. Zibetti, Charlot & Rix 2009).

We have independently analysed the SDSS images of the sample and performed elliptical isophote fitting, from which we have derived average ellipticity ϵ and position angle PA with the procedure described in Consolandi et al. (2016). With this re-processing we were able to fix a few cases of apparently wrong estimates of PA and ellipticity reported in the tables of Walcher et al. (2014). From integrated photometry in elliptical apertures we have further derived total magnitudes and effective semimajor axes, defined as the semimajor axis (SMA) of the elliptical aperture enclosing half of the total flux and denoted by R_e.

Velocity dispersions, σ_e are available for 54 galaxies from Falcón-Barroso et al. (2017), while for the remaining 15 galaxies measurements are computed in this work by JF-B. The velocity dispersions are derived from integrated spectra within the 1 R_e elliptical aperture, obtained in the V1200 setup (blue, high-resolution) of CALIFA. Hence these are effectively light-weighted mean velocity dispersions within R_e.

Fig. 1 displays the distributions in M_* and σ_e for the sample as a whole and for the subsamples of ellipticals (E, in purple) and S0 (in orange). We span a range between ∼100 and ∼ 300 km s^{-1} in σ_e. In terms of M_* the range covered spans from 2 × 10^{10} to 7 × 10^{11} M$_\odot$, thus extending a factor ∼3 beyond the limit of representativeness of CALIFA (in fact, galaxies with $M_* > 2.5 \cdot 10^{11}$ M$_\odot$ are underrepresented in the main CALIFA sample). In Table 1 we report the number of galaxies, the median stellar mass M_*, and the median velocity dispersion σ_e for the full sample and

Table 1. Characterization of the sample and the subsamples in terms of stellar mass and velocity dispersion.

Sample	Boundaries	N	median $\log M_*$ $\log \mathrm{M}_\odot$	median σ_e $\mathrm{km \, s^{-1}}$
All		69	11.05	185
E		48	11.18	189
S0		21	10.93	178
E (mass-matched w/S0)	$M_*/\mathrm{M}_\odot < 2 \times 10^{11}$ $\log M_*/\mathrm{M}_\odot < 11.3$	28	11.00	174
All, low-M_*	$M_*/\mathrm{M}_\odot < 7.9 \times 10^{10}$ $\log M_*/\mathrm{M}_\odot < 10.9$	16	10.68	162
All, mid-M_*	$7.9 \times 10^{10} \leq M_*/\mathrm{M}_\odot < 2 \times 10^{11}$ $10.9 \leq \log M_*/\mathrm{M}_\odot < 11.3$	31	11.02	175
All, high-M_*	$M_*/\mathrm{M}_\odot \geq 2 \times 10^{11}$ $\log M_*/\mathrm{M}_\odot \geq 11.3$	22	11.46	236
All, low-σ_e	$\sigma_\mathrm{e}/\mathrm{km \, s^{-1}} < 170$	21	10.92	154
All, mid-σ_e	$170 \leq \sigma_\mathrm{e}/\mathrm{km \, s^{-1}} < 210$	25	11.02	182
All, high-σ_e	$\sigma_\mathrm{e}/\mathrm{km \, s^{-1}} \geq 210$	23	11.44	236

for different subsamples, selected in morphology, M_* or σ_e. From both Fig. 1 and Table 1 it is apparent that E's and S0's span different ranges in M_* and σ_e. In particular S0's are biased low in M_* with respect to E's. Therefore we define a subsample of E's with a limit of $M_* < 2 \times 10^{11} \mathrm{M}_\odot$ (corresponding to the 90th percentile in the M_* distribution of S0's) in order to control for M_* when comparing S0's with E's.

While there is an obvious correlation between M_* and σ_e, the scatter is significant, especially for S0's. This justifies the distinct analysis of the dependence on the two parameters. In the following sections we will consider three bins in both M_* and σ_e, with the boundaries reported in Table 1 and indicated by dashed lines in Fig. 1.

3 STELLAR POPULATION ANALYSIS IN 2D

3.1 Method

We approach the analysis of the stellar populations in our galaxy sample by mapping their 2D distribution. We follow the Bayesian method already adopted in Z17, which builds on the original work by Gallazzi et al. (2005), with a few modifications that will be highlighted in the next paragraphs. At any given 'pixel' of a given galaxy we measure a set of observables from the CALIFA IFS and the SDSS imaging. The same observables are measured on an extensive suite of spectral models, each of them having a set of associated physical parameters (e.g. light-weighted age, metallicity etc.). The likelihood of each set of real observables (with associated errors) for a given model i, is assumed to be

$$\mathcal{L}_i \propto \exp(-\chi_i^2/2), \tag{1}$$

with the standard definition of χ^2. The (posterior) probability distribution function (PDF) of a physical parameter associated to the models is derived by weighing the prior distribution of models in that parameter by their likelihood $\mathcal{L}_i$, following Bayes' theorem.

In this paper we focus on two light-weighted mean properties of the stellar populations, specifically the r-band-light-weighted mean age Age_* and metallicity Z_* (see Z17 section 2.3 and equations 4 and 6 therein). Mean quantities are computed from the linear

parameters,[2] i.e. age in Gyr and Z as metal abundance ratio normalized to the solar value of 0.02. We also derive the stellar mass surface density based on the PDF of the scaling factor that one must apply to a 1–$\mathrm{M}_\odot$ model spectrum in order to match the SDSS photometry.

The spectral library adopted in this study is the same as the one used in Z17, with the only exception of a different prior on the dust attenuation parameters. It includes 500 000 models generated from random star-formation histories (SFH), metal-enrichment histories, and effective dust attenuation. The base spectral library of simple stellar populations (SSPs) is the Bruzual & Charlot (2003) in the 2016 revised version (CB16), which adopts the Chabrier (2003) initial mass function, an updated treatment of evolved stars (Marigo et al. 2013), and the MILES stellar spectral library (Sánchez-Blázquez et al. 2006; Falcón-Barroso et al. 2011). SFHs á la Sandage (1986) are adopted for the continuous component: $\mathrm{SFR}_\tau(t) \propto \frac{t}{\tau} \exp\left(-\frac{t^2}{2\tau^2}\right)$. A random burst component is also added on the top of it. Up to six burst can be added, with an intensity (i.e. fraction of stars formed relative to the total formed in the continuum component) ranging between 10^{-3} and 2. For bursts with age $\mathrm{age_{burst}} < 10^8$ yr, the maximum fraction of stars formed is gradually decreased from 2 to $10^{-2.5}$ at $\mathrm{age_{burst}} = 10^5$ yr, in order to avoid recent bursts that totally overshine the rest of the SFH.

A simple chemical enrichment history is also implemented. The metallicity of the stars formed at time t increases from an initial value Z_{*0} (randomly generated between 0.02 and 0.05 $\mathrm{Z}_\odot$) to a final value $Z_{* \, \mathrm{final}}$ (also randomly generated between Z_{*0} and 2.5 $\mathrm{Z}_\odot$) as a function of the time-integrated mass fraction, according to the law:

$$Z_*(t) = Z_*(M(t)) = Z_{* \, \mathrm{final}} - (Z_{* \, \mathrm{final}} - Z_{*0})$$
$$\times \left(1 - \frac{M(t)}{M_{\mathrm{final}}}\right)^\alpha, \alpha > 0 \tag{2}$$

α is a random shape parameter that describes how quickly the enrichment occurs, from instantaneously ($\alpha \gg 1$) to delayed ($\alpha < 1$).

---

[2]This is especially relevant to properly compare the present results with works in literature where log quantities are averaged. See also discussion in Appendix B (available online).

We mimic the stochasticity of the bursts by assigning each burst a metallicity $Z_{*\mathrm{burst}}$ equal to the metallicity of stars formed in the continuous mode at the time of the burst, $Z_*(t = t_{\mathrm{obs}} - \mathrm{age_{burst}})$, plus a random offset taken from a lognormal distribution with $\sigma = 0.2$ dex.

Dust attenuation is implemented following Charlot & Fall (2000), who assume two components of dust: a diffuse ISM with an effective attenuation law that goes as the wavelength $\lambda^{-0.7}$, and the dust in the birth cloud (BC), which embeds young stars (age $\leq 10^7$ yr) only, with an effective attenuation law that goes as $\lambda^{-1.3}$. Young stars, therefore, suffer attenuation from both components, yielding a total optical depth in V-band of τ_V, with a fraction μ attributed to the diffuse ISM, and a fraction $1 - \mu$ attributed to the BC. Older stars are effectively attenuated only by the diffuse ISM, hence with a V-band optical depth of $\mu\tau_V$. The two free parameters, τ_V and μ are randomly generated with probability distributions, which are flat at low values and drop exponentially to 0 between $\tau_V = 4$ and 6, and between $\mu = 0.5$ and 1, respectively, as in da Cunha, Charlot & Elbaz (2008).

For this study we have allowed for a much larger fraction of dust-free models, i.e. 90 per cent, than the one adopted in Z17, 25 per cent. This choice is justified by the restricted sample of ETGs analysed here. ETGs are known to have a much lower dust content than spirals. For instance, in the Herschel Reference Sample (HRS), Smith et al. (2012) show that the ratio of dust over stellar mass is lower by a factor 50 in ETGs with respect to spirals, on average, and the detection rate of ellipticals at $250\,\mu$m is only 24 per cent. With this prior we are able to provide tighter constraints (and lower residual biases) wherever dust is not required, by limiting the impact of dust on the dust–age–metallicity degeneracy. On the other hand, despite the small fraction of dusty models, we are able to correctly identify dust lanes and avoid significant biases in the (few) dusty regions. Although visual inspection has shown us that the extent of such regions is reduced with respect to what we get with the Z17 prior, the number of pixels affected is small enough to produce negligible effects on the azimuthally averaged profiles of age and metallicity (see below).

It is important to stress that we do not aim at retrieving or fitting the full complexity of these parameters in the real galaxies. Rather we want to include the maximum possible degree of complexity in our models, so as to properly take into account the parameter degeneracies on the estimates and uncertainties of the key physical quantities in which we are interested, namely *the light-weighted mean age and metallicity of the stellar populations and the stellar mass surface density*.

The key observables from which we derive the likelihood $\mathcal{L}_i$ are four stellar absorption indices and the photometric fluxes in the five SDSS bands, *ugriz*. As absorption indices we use the Balmer indices, $H\beta$ and $H\delta_A + H\gamma_A$, mainly age-sensitive, and two (mostly) metal-sensitive composite indices that show minimal dependence on α-element abundance relative to iron-peak elements ([Mg$_2$Fe] and [MgFe]$'$). As opposed to previous works and to Z17 in particular, we do not employ the D4000$_n$ break, despite of its well proved sensitivity to age. The reason for this choice resides in the limited sensitivity and, most important, sky-subtraction accuracy, of the CALIFA data set bluewards of 4000 Å. At fixed limiting surface brightness in r-band (or fixed limiting stellar mass surface density), ETGs display the lowest levels of surface brightness bluewards of 4000 Å with respect to the general galaxy population, due to their red spectral energy distribution and extreme D4000$_n$ break strength. Therefore even small residual pedestals from the sky subtraction can significantly affect the measurement of D4000$_n$ in the outskirts of

these galaxies, leading to biases that depend on surface brightness (radius). Since the main goal of this paper is to derive reliable and consistent stellar population profiles, we rather not use D4000$_n$. It must be noted that the $u - g$ colour is partly redundant with D4000$_n$, so the information encoded in the break is only minimally lost. For galaxies that do not display any apparent problem in the D4000$_n$ map, we find that age and metallicity maps that are obtained with and without D4000$_n$ are very consistent with each other, with slightly larger uncertainties when D4000$_n$ is excluded. On the other hand, when problems in the D4000$_n$ map are apparent, differences in the physical parameters are seen, and associated uncertainties are larger when D4000$_n$ is included.

Simulations of typical CALIFA-SDSS observations show that systematic biases at the level of a few 0.01 dex may be present in both age and metallicity estimates, for the range of physical parameter relevant to ETGs. The largest biases are expected for $\log Z_*/Z_\odot \gtrsim 0.3$: since in the models there is a hard boundary for Z_* at $\log Z_*/Z_\odot = 0.4$, the PDFs are skewed towards lower values and a bias is generated. As a consequence of the age–metallicity degeneracy, an opposite bias is induced in the age estimates. Therefore, at the highest stellar metallicity we expect to have underestimated metallicity by a few 0.01 dex up to 0.05 dex and, correspondingly, overestimated ages by a few 0.01 dex up to 0.1 dex. A similar, although smaller, 'boundary' effect is observed at the largest ages (Age$_* \gtrsim 8$ Gyr) for $\log Z_*/Z_\odot \lesssim 0.1$. In this regime, ages are underestimated by up to 0.05 dex with a corresponding overestimate of Z_* by up to 0.05–0.07 dex. We will discuss the implication of these residual biases on the stellar population profiles in Section 4.4.

3.2 CALIFA-SDSS data processing

The first step to study the dependence of stellar population properties on radial galactocentric distance and on surface brightness/stellar-mass density is to create 2D maps of age and metallicity as well as of stellar mass surface density, μ_*. In order to achieve this, we create maps of surface brightness in the five SDSS bands, and of index strength for the set defined in the previous section. These maps are matched in terms of sampling and effective resolution, following the procedure detailed in Z17. More specifically, we degrade the native resolution of the SDSS images to match the spatial resolution of the CALIFA data cubes (PSF FWHM ~ 2.57 arcsec). Given the redshift distribution of our sample, this angular resolution translates into a typical physical resolution of $\lesssim 1$ kpc. In terms of effective radius, we typically resolve $\lesssim 0.1 R_e$. More quantitatively, we consider as PSF radius the half-width at half-maximum (HWHM, i.e. 0.5 FWHM) of the PSF. The median ratio of PSF radius to R_e is 0.08; 70 per cent of the sample have this ratio < 0.1, and the remaining 30 per cent between 0.1 and 0.2 (see the full distribution in Fig. A1 of Appendix A, available online). Hence we conclude that we have sufficient spatial resolution to resolve the stellar population trends down to at least 0.2 R_e for the full sample, and down to 0.1R_e for a representative majority of galaxies.

The stellar population analysis requires moderately high signal-to-noise ratio (SNR) in order to keep uncertainties below $0.2 - 0.3$ dex: a typical SNR of ~ 15 per Å (20 per spectral pixel) is sufficient to this goal for CALIFA COMBO spectra, as we verified both on simulations and on real data. Since the SNR actually delivered by CALIFA is typically lower than that for most galaxies at galactocentric distances beyond 1R_e, we apply a spatially adaptive smoothing of the cubes, following the approach of ADAPTSMOOTH Zibetti 2009; Zibetti et al. 2009). As in Z17

we choose a target SNR of 20 and a maximum kernel radius of 5 arcsec.[3] We further restrict the analysis to spaxels with r-band surface brightness $\mu_r \leq 22.5\,\mathrm{mag\,arcsec^{-2}}$, as determined on the matched SDSS images, in order to define a highly complete set of regions (completeness > 90 per cent) over a well-defined range in surface brightness (see Z17).

The next step in the processing is to derive the kinematic parameters (line-of-sight velocity v and velocity dispersion σ) at every spaxel and decouple possible nebular emission lines from the underlying stellar continuum. This is performed using an iterative procedure based on PPXF (Cappellari & Emsellem 2004) and GANDALF (Sarzi et al. 2006). We subtract the best-fit emission lines that are detected with an amplitude-over-noise ratio larger than 2, from the original spectrum. Spectral absorption indices are measured on this 'clean' spectrum in the precise rest-frame defined by v, without applying any correction for σ. The effect of σ-broadening on the indices is taken into account by directly modelling it in the models. In fact, in order to compute the χ^2 of each model, the observed indices are compared to model indices measured on model spectra that have previously been convolved to match the effective resolution and σ in the observations (see Gallazzi et al. 2005).

The broad-band SDSS photometric fluxes are cleaned by the emission line contributions determined with GANDALF. In the χ^2 computation, these fluxes are compared with the synthetic fluxes extracted from the model spectra using properly shifted filter response functions that match the redshift and Doppler v-shift of each spaxel.

From the posterior PDFs derived as described in the previous sections, we obtain maps of median-likelihood stellar mass surface density μ_*, r-band-light-weighted age Age$_*$ and metallicity Z_*. At each spaxel, the fiducial value of the quantity is taken as the median of the PDF, while the uncertainty is given by half of the 16th $-$ 84th percentile range (corresponding to $\pm 1\sigma$ in Gaussian approximation). It must be noted that this uncertainty includes both measurement errors as well as the intrinsic uncertainty due to the degenerate effect of different SFHs and chemical enrichment histories on the observable quantities. For this reason, uncertainties on the estimates of light-weighted age and metallicity in individual spaxels can hardly drop below 0.1 dex, no matter how much we shrink the error bars on the observable quantities.

4 STELLAR POPULATION PROFILES

In the following subsections we describe three different kinds of profiles for stellar population parameters, which are shown in Fig. 2, with Z_* in the left-hand column and Age$_*$ in the right one: azimuthally averaged elliptical radial profiles (top row), profiles as a function of r-band surface brightness μ_r (mid row), and profiles as a function of stellar-mass surface density μ_* (bottom row). Each orange line corresponds to a galaxy, with its hue, ranging from light to dark orange, displaying the light-weighted average velocity dispersion within $1\,R_e$, σ_e. The blue solid line represents the median of all galaxies at any given abscissa bin, the dashed blue lines are the corresponding 16th and 84th percentiles. Half of this percentile range is plotted in the bottom panels and represents the scatter of the

---

[3] In practice, smoothing is only applied at SMA $\gtrsim 1\,R_e$, with a kernel radius that increases radially following the declining surface brightness. The spatial resolution is therefore not affected in the inner regions, but only in the outer regions where gradients are already intrinsically milder.

sample. The top panel of each plot displays the number of galaxies contributing with their profile at any given abscissa bin.

From the analysis of the PDF, typical uncertainties on age and metallicity in individual spaxels are both approximately 0.15 dex, including random measurement errors and systematic contributions inherent to the modelling. An independent measurement of the uncertainty is provided by the scatter in the estimates for individual spaxels inside the bins used to create the profiles. For age determination the scatter is distributed with a median of 0.08 dex, between 0.04 dex and 0.12 dex. For Z_* determinations the median scatter is 0.1 dex and varies between 0.05 dex and 0.15 dex approximately. In both cases, the scatter is less than the estimated error in individual spaxels. This can be understood as a consequence of spaxel correlations and, most important, of systematic uncertainties being included in the error estimate based on our Bayesian analysis. If we make a rough evaluation (neglecting spaxel covariance) of the random uncertainty in each bin as the rms around the median divided by the square root of the number of spaxels, we end up with estimates of the order of a few 0.01 dex at most, thus well below our systematic uncertainties.

## 4.1 Azimuthally averaged elliptical profiles

Azimuthally averaged elliptical profiles are obtained by binning the maps according to the semimajor axis (SMA) of elliptical annuli centred on the galaxy's nucleus, with ellipticity ϵ and position angle PA as determined in Section 2. In each annulus we consider the median value of the stellar population parameter (Z_* and Age$_*$, respectively). This is plotted against the average (midpoint) value of SMA normalized to the R_e. Because of the limited field of view or of masked spaxels (due, e.g. to foreground stars or artefacts), only a portion of spaxels may be available in a given elliptical annulus. If the representativeness drops below 2/3, the profile is drawn with a dotted line and those radial bins are not considered for the computation of the median and percentiles of the sample (blue lines). Within $1\,R_e$ we are highly complete, with $> 65/69 = 94$ per cent of galaxies contributing in this range. The completeness drops to $51/69 = 74$ per cent at $1.5\,R_e$ and then to $32/69 = 46$ per cent at $2\,R_e$.

The stellar metallicity Z_* monotonically decreases as a function of SMA in a very consistent way for all galaxies (top left-hand panel of Fig. 2). The gradient is steeper within $1\,R_e$, then the profiles flatten out beyond that radius. Z_* decreases by ~ 0.3 dex (roughly a factor 2) going from the nucleus to $1\,R_e$. The scatter of the sample around the median is remarkably small, typically 0.1 dex (~ 25 per cent) and decreases to ~ 0.05 (~ 12 per cent) from $0.5\,R_e$ towards the centre. Note that such a scatter is smaller than expected from the systematic uncertainties in our simulations, which further indicates a strong regularity (universality) in the metallicity profiles of ETGs. We also note a systematic tendency for the profiles of higher-σ_e galaxies (darker orange hue) to lay above those of lower-σ_e galaxies (lighter orange hue). We will quantify this effect better in Section 5.

In terms of light-weighted age Age$_*$, profiles are overall flat (top right-hand panel of Fig. 2). The median profile spans a range of ~ 0.15 dex only, between 6.8 and 8.9 Gyr. Remarkably, the median age profile of the sample is *not* monotonic, rather U-shaped. All galaxies display the largest ages beyond $1\,R_e$. This maximum age of ~ 8.9 Gyr is roughly constant for all galaxies, with a sample rms of $\lesssim 0.07$ dex. Age decreases from $1\,R_e$ inwards to $0.5\,R_e$. Below $0.5\,R_e$ age profiles display a larger degree of diversity, as witnessed by the scatter, which increases to ~ 0.1 dex (up to 0.2 dex in the
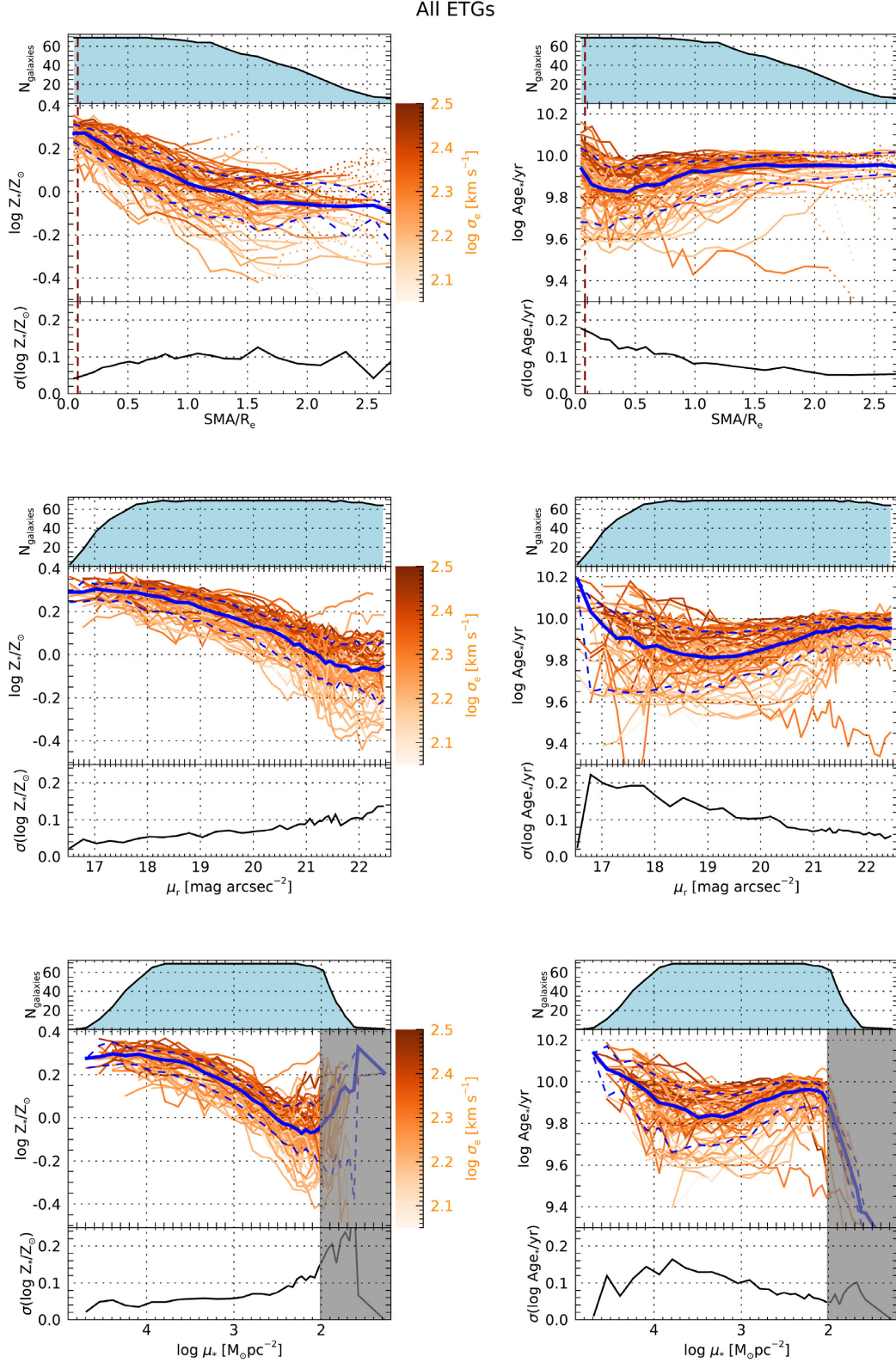
Figure 2. Profiles of light-weighted stellar metallicity Z_* (*left-hand column*) and stellar age Age$_*$ (*right-hand column*) as a function of different quantities for the full sample of 69 ETGs. In the *top row* quantities are plotted as a function of the elliptical semimajor axis (SMA) normalized by the half-light semimajor axis R_e, as a function of the r-band surface brightness μ_r in the *mid row*, and as a function of the stellar mass surface density μ_* in the *bottom row*. The main panel of each plot displays the profile of each individual galaxy, colour-coded according to the velocity dispersion σ_e within 1 R_e (see side colourbar). In the top row, dotted lines indicate completeness <0.67, the vertical dashed lines mark the median PSF radius (HWHM). The blue lines represent the sample median (solid line) and the 16th and 84th percentiles (dashed lines), only profiles with completeness >0.67 contribute. In the top and bottom panels of each plot we report the number of contributing galaxies and the scatter of the quantity on y-axis around the median, respectively.

centre). On average, moving to the centre, galaxies get as old as in the outskirts, although this trend is highly variable on a galaxy-to-galaxy basis and correlates with global quantities such as σ_e, as we will show in Section 5. A dependence of the age profiles on σ_e is already visible by looking at the dominant hue of the lines, indicating that galaxies with higher velocity dispersion tend to have overall larger ages and typically flatter profiles than galaxies with lower velocity dispersion.

The U-shape of the age profile is indeed a common feature to the majority of galaxies. In fact, from visual inspection of the individual profiles, we find: 28 galaxies that are fully consistent with the U-shape having a minimum at $0.4R_e$ 11 galaxies with U-shape but minimum inside $0.3R_e$; 6 galaxies with U-shape but minimum outside $0.4R_e$; 3 galaxies with an extended plateau around the minimum; 3 galaxies with a noisy profile that is consistent with the median U-shape; the remaining 18 galaxies not showing any evidence for U-shape or inconsistent with that. In summary, 51 out of 69 galaxies display U-shaped age profiles, with some variations in the position of the minimum.

4.2 Profiles in surface brightness and stellar-mass surface density

Profiles in r-band surface brightness (SB, μ_r) and stellar-mass surface density (μ_*) are obtained by binning the spaxels in μ_r and μ_*, respectively. In Fig. 2, the median value of the stellar population property inside the bin is plotted against the median μ_r (middle row) and μ_* (bottom row), with metallicity in the left-hand column and age on the right-hand column.

As a function of μ_r (mid row), essentially all galaxies are represented for $\mu_r > 18$ mag arcsec^{-2} down to the selection limit of 22 mag arcsec^{-2}. A decreasing number of galaxies reach μ_r as bright as $\sim 16.5 - 17$ mag arcsec^{-2}, as a consequence of the different shapes of the surface brightness profiles of the ETGs in our sample.

As a function of μ_* (bottom row), we note that the cut-off at low stellar-mass surface density is less abrupt than at low SB, due to errors in M/L. Since we apply a sharp selection cut at $\mu_r = 22$ mag arcsec^{-2}, which corresponds on average to $\log \mu_* \sim 2$, the tail of the distribution below this value is contributed (mainly) by spaxels whose M/L is underestimated due to errors. Hence spaxels with $\log \mu_* \lesssim 2$ are characterized by biased estimates of stellar population properties. In particular, since errors in M/L are correlated with errors in Age$_*$ and, in turn, errors in Z_* are anticorrelated with errors in Age$_*$, points below the limiting μ_* of $10^2 M_\odot$ pc^{-2} are severely biased also in Age$_*$ (downturning profiles) and Z_* (up-turning profiles). For this reason, that entire region must be neglected and is shaded in grey in Fig. 2.

Profiles of Z_* stay almost flat in the highest SB/density regions and then decrease with steeper and steeper derivative as we move to lower SB/density. The scatter is around or slightly above 0.05 dex in the (inner) higher-SB/density regions, over almost 2 orders of magnitudes in SB/density, and increases to $0.1 - 0.15$ dex only in the (outer) low-SB/density regions. As already noted for the radial metallicity profiles, the scatter (especially in the inner, higher SB/density regions) is tiny compared to possible systematic uncertainties and points to a high degree of universality in the dependence of Z_* on radius and on μ_r or μ_*. Looking at the profiles of the individual galaxies, it is apparent that there is a significant dependence of the Z_* profiles on the velocity dispersion σ_e, which is much more evident than in the case of radial elliptical profiles. There is in fact an average shift of the profiles of galaxies with
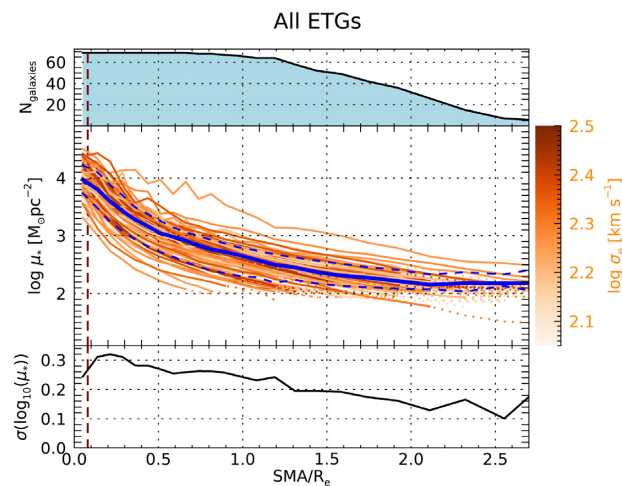
Figure 3. Profiles of stellar mass surface density μ_* as a function of the elliptical semimajor axis (SMA) normalized by the half-light semimajor axis R_e, for the full sample of 69 ETGs. The main panel displays the profile of each individual galaxy, colour-coded according to the velocity dispersion σ_e within $1R_e$ (see side colourbar). The blue lines represent the sample median (solid line) and the 16th and 84th percentiles (dashed lines). In the top and bottom panels we report the number of contributing galaxies and the scatter of $\log \mu_*$ around the median, respectively. The vertical dashed line marks the median PSF radius (HWHM). For a reference, at SMA $= R_e$ the median $\mu_*(R_e)$ is $10^{2.65}$ M$_\odot$ pc^{-2}, and a μ_* of 10^3 M$_\odot$ pc^{-2} corresponds to $0.57 R_e$.

higher σ_e towards larger Z_*, over a range that is comparable with the scatter around the median profile.

Stellar light-weighted age profiles display a U-shape, even more evident than what is seen in radial profiles, with a minimum corresponding to ~ 6.8 Gyr at $\mu_r \sim 19$ mag arcsec^{-2} or $\log \mu_*/M_\odot pc^2 \sim 3.5$. The scatter is typically larger than the one displayed in Z_*, and decreases from ~ 0.15 dex in the brightest regions to $\lesssim 0.1$ dex when we move to regions fainter than 20 mag arcsec^{-2} or $\log \mu_*/M_\odot pc^2 < 3$. Overall this is consistent with the radial profiles, although we note that by binning in SB/density, the brightest/densest of the central regions reach older ages than fainter or less dense ones, even older than the outer regions, and exceed 10 Gyr. We note also a trend for profiles of higher-σ_e galaxies to display overall larger ages and a less deep minimum (i.e. flatter shape).

Apart from the above-mentioned difference at the dim end due to measurement effects, profiles as a function of μ_r and of μ_* mirror each other very closely. This is not surprising if one considers that M/L ratios span a small dynamical range for old and metal-rich stellar population like those in ETGs (e.g. Bruzual & Charlot 2003, their fig. 1), and therefore μ_r and μ_* trace each other very well. For the rest of the paper we will no longer discuss profiles in μ_r and refer instead to profiles in μ_*, the latter being a more fundamental physical quantity.

4.3 Relating azimuthally averaged elliptical profiles and profiles in stellar-mass surface density

Radial elliptical profiles and profiles in μ_* are obviously related one to the other via radial elliptical profiles of stellar surface mass density. We plot them in Fig. 3 with the same graphic format as for Fig. 2.

All profiles but a few display similar shapes, i.e. the typical cuspy de Vaucouleurs (1948) profiles. As a result, at first-order approxi-

mation, radial elliptical profiles translate into profiles in μ_* that are more stretched in the inner, brighter parts, and more compressed in the outer, faint parts. This mere 'coordinate' transformation explains the basic difference in shape between these two kinds of profiles in Fig. 2.

The normalization of the profiles, on the other hand, exhibits a significant scatter of $\sim 0.25 - 0.3$ dex inside $1R_e$. Because of the cut we apply in surface brightness, we note that we miss an increasing number of galaxies as we move beyond $1R_e$ and the sample becomes more and more biased towards the galaxies of higher average surface brightness/mass density. The tight $\mu_* - Z_*$ relation presented in the bottom left-hand panel plot of Fig. 2, which is unaffected by selection biases, hence implies that the parts of the radial metallicity profiles missing at SMA $> 1R_e$ are preferentially low-metallicity. In turn, this may (i) bias the median radial metallicity profile of the sample beyond $1R_e$ to appear flatter than it is in reality and (ii) artificially decrease the scatter. On the other hand, the *individual* profiles that extend far enough display a similar flattening as the median profile, hence reassuring about its real nature.

Concerning the age profiles, we note that beyond $1R_e \log \mu_*$ gets smaller than 3, a regime where we observe a mild anticorrelation between Age$_*$ and μ_*. Therefore, the outer radial age profiles miss preferentially larger ages and may be biased low. However, since the derivative of Age$_*$ with respect to μ_* approaches 0 as we move to low surface mass density, we do not expect this bias to significantly alter the shape of the median radial profile.

Fig. 2 highlights the existence of both an SMA $- Z_*$ relation and of a $\mu_* - Z_*$ relation. Both relations are remarkably tight, especially in the inner/high-surface-density regions. Still it makes sense to investigate whether one is more 'fundamental' than the other. We consider the scatter around the median relations in a range where we are highly complete and the scatter is roughly constant, that is $0.5 R_e <$ SMA $< R_e$ corresponding to $3.05 > \log \mu_* > 2.65$ (see Fig. 3). In these regions the scatter around the SMA $- Z_*$ relation is ~ 0.10 dex while the scatter around the $\mu_* - Z_*$ relation is ~ 0.07 dex. A clearly lower scatter in the $\mu_* - Z_*$ relation is apparent even if we extend the range to include the inner/higher-surface-density regions (down to $0.1 R_e$ or up to 4 in $\log \mu_*$): the typical scatter in the $\mu_* - Z_*$ relation is always around ~ 0.06 dex, while the scatter in the SMA $- Z_*$ relation drops below 0.075 dex only inside $0.3R_e$. In other words, μ_* is a better predictor of the local Z_* than the radial distance from the centre, thus supporting the idea that the $\mu_* - Z_*$ relation is the driving one, with the SMA $- Z_*$ relation being a consequence of the former one and of the quasi-universal shape of the SMA $- \mu_*$ profiles. In fact, one can work out that the larger scatter in the SMA $- Z_*$ relation with respect to the $\mu_* - Z_*$ relation, within $1 R_e$, is quantitatively consistent with this hypothesis.

4.4 Impact of biases in stellar population profiles

As mentioned at the end of Section 3, biases in the inferences of stellar population parameters may arise as one approaches the physical limits of the parameter space covered by the models. In the actual profiles we may be possibly biased in the central (SMA $< 0.3 - 0.4 R_e$) and most dense regions ($\log \mu_* \gtrsim 3.3$), where $\log Z_*/Z_\odot \gtrsim 0.2 - 0.3$. Due to the hard limit in $\log Z_*/Z_\odot = 0.4$ present in our library, in those regions, we might be underestimating the true metallicity by a few 0.01 dex up to 0.05 dex. We might also correspondingly overestimate the true age by a few 0.01 dex up to 0.1 dex, although for ages as high as $\sim 8 - 10$ Gyr the effect is expected to be even milder. As a consequence, metallicity profiles in

the central/densest regions might be steeper in reality; in particular, the stark flattening observed in the profiles versus μ_* might be partly an artefact. On the contrary, the central age cusp might be enhanced with respect to the reality.

On the other hand, in the less dense regions, typically beyond $1R_e$, for ages $\gtrsim 8$ Gyr and relatively low metallicity we might be biased low in age by a few 0.01 dex (see last paragraph of Section 3) and, correspondingly, we might be biased high in Z_* by a few 0.01 dex. As a consequence, the age 'plateau' at large distances/low densities might be slightly higher in reality, and the metallicity profiles somewhat steeper. Note that a negative correction (i.e. to steeper slopes) to the radial derivative of metallicity is also expected from the surface brightness cut discussed in the previous section.

Considering the maximum amplitude of these biases, we do not expect significant changes in the shapes of the profiles plotted in Fig. 2, rather just small offsets and changes of slopes. In particular, all considerations and conclusions about the qualitative shapes of the profiles, the scatter, and the existence of tight (quasi-)universal relations are robust against the possible biases of the stellar population analysis.

More systematic effects related to the choices of averaging linear quantities rather than their logarithm to estimate Age$_*$ and Z_*, and of using a fixed universal IMF from Chabrier (2003) are illustrated in Appendix B (available online). Although different choices/assumptions in these respects may change our results *quantitatively*, the *qualitative* picture and the trends that emerge from our analysis are robust.

5 AVERAGED STELLAR POPULATION PROFILES

In this section we analyse how stellar population profiles (both in SMA and in μ_*) depend on global galaxy properties, namely on the stellar velocity dispersion within R_e, σ_e, on the total stellar mass, M_*, and on the morphology (E versus S0). To this goal, we bin galaxies in different classes and, in each of them, we proceed to compute the median averaged profiles and percentiles, as we did for the full sample in Fig. 2. In particular, individual profiles contribute only as long as spaxel completeness is larger than $2/3 = 0.67$.

The different subsamples are defined in Table 1 and are plotted in different colours in Figs 4 (radial profiles) and 5 (profiles in μ_*), according to the corresponding legends. As a reference, all plots report the median profiles of the unbinned sample (all ETGs in the top three plots, all Es in the bottom one, respectively) as solid blue line, with shaded blue regions covering the 16th $-$ 84th percentile range. The same two percentiles are shown for the subsamples as dashed lines in the corresponding colour. The green-shaded regions indicate the range where less than 1/3 of the galaxies contribute.

5.1 Averages in M_* and σ_e bins

Radial profiles display a clear dependence on σ_e for both age and metallicity, as one can see in the top panels of Fig. 4 (full sample of 'All ETGs' in bins of σ_e). At low and intermediate σ_e the median metallicity profiles are very similar, but are significantly different from the metallicity profile of galaxies with $\sigma_e \geq 210$ km s^{-1}. High-σ_e galaxies share with lower-σ_e galaxies very similar Z_* in the central regions, but their decrease of Z_* with *SMA* is slower and results in a difference of ~ 0.1 dex in Z_* at ~ 1.5 R$_e$ with respect to lower-σ_e galaxies. The effect of σ_e is particularly dramatic on age profiles. All galaxies share a very similar old age of ~ 8.9 Gyr beyond ~ 1.5 R$_e$, yet with a small but significant age offset correlated with σ_e. Inside
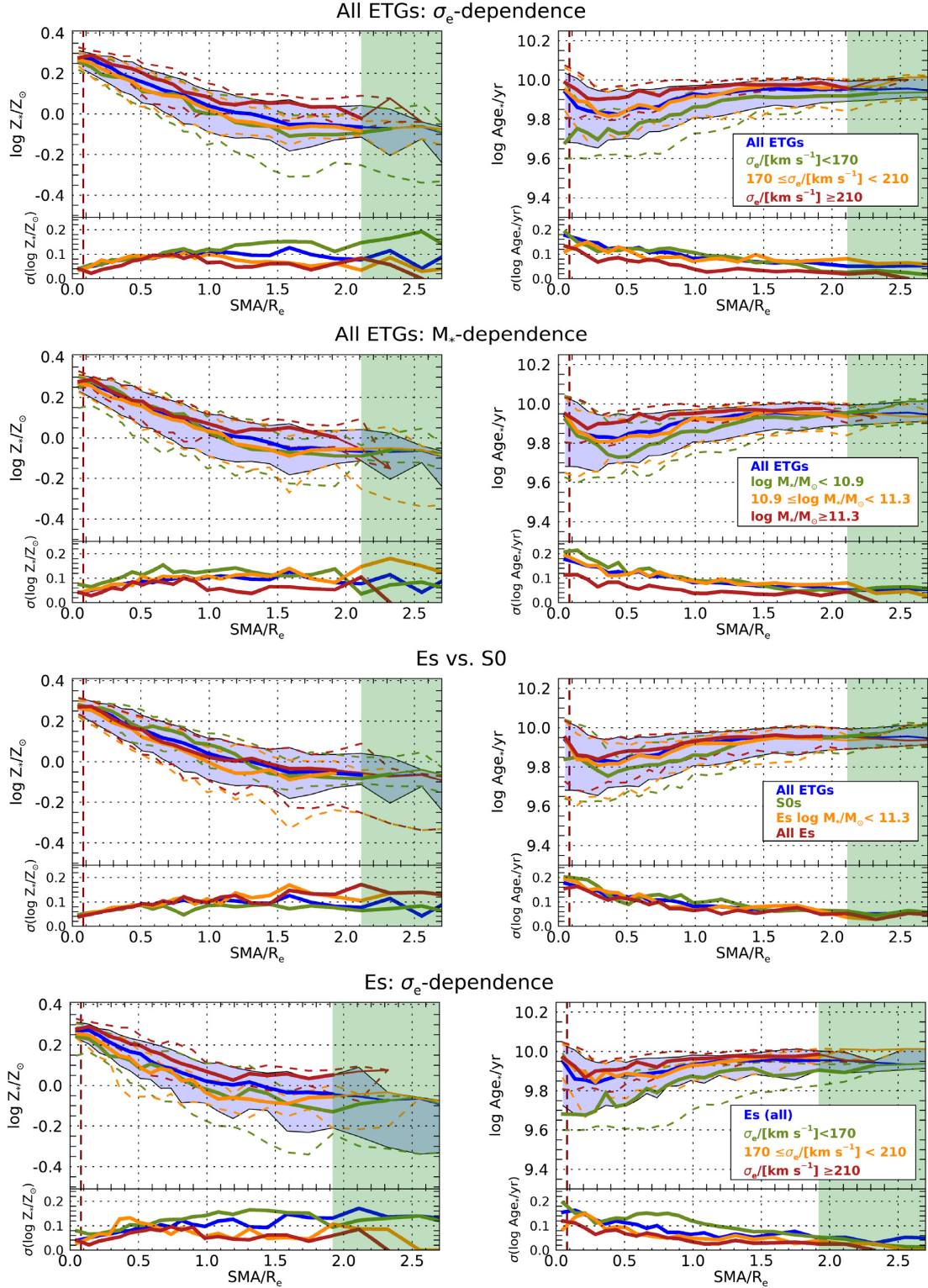
Figure 4. Azimuthally averaged radial profiles of light-weighted stellar metallicity Z_* (*left-hand column*) and stellar age Age_* (*right-hand column*) for different galaxy subsamples. From the top row to the bottom: all ETGs binned according to their σ_e; all ETGs binned according to their M_*; Es versus S0 versus Es in the corresponding M_* range of S0; only Es binned according to their σ_e. The main panel of each plot displays the median profile of each bin (solid lines) and the 16th and 84th percentiles (dashed lines), colour-coded according to the legend. The blue line and shaded area correspond to the median and interpercentile range of the full unbinned sample (all ETGs for the first three rows, all Es only for the bottom row), and are reported for reference in all plots. The green-shaded regions indicate the range where less than 1/3 of the galaxies in the unbinned sample contribute. Line representing less than 1/3 of galaxies in a given subsample are thin. In the bottom panels of each plot we report the scatter of individual profiles around the median of each subsample. The vertical dashed lines mark the median PSF radius (HWHM). *Most notably, we observe that σ_e is the main parameter that modulates the shape of the profiles, while morphology plays a secondary role and M_* appears to control the shape of the profiles only via its correlation with σ_e.*
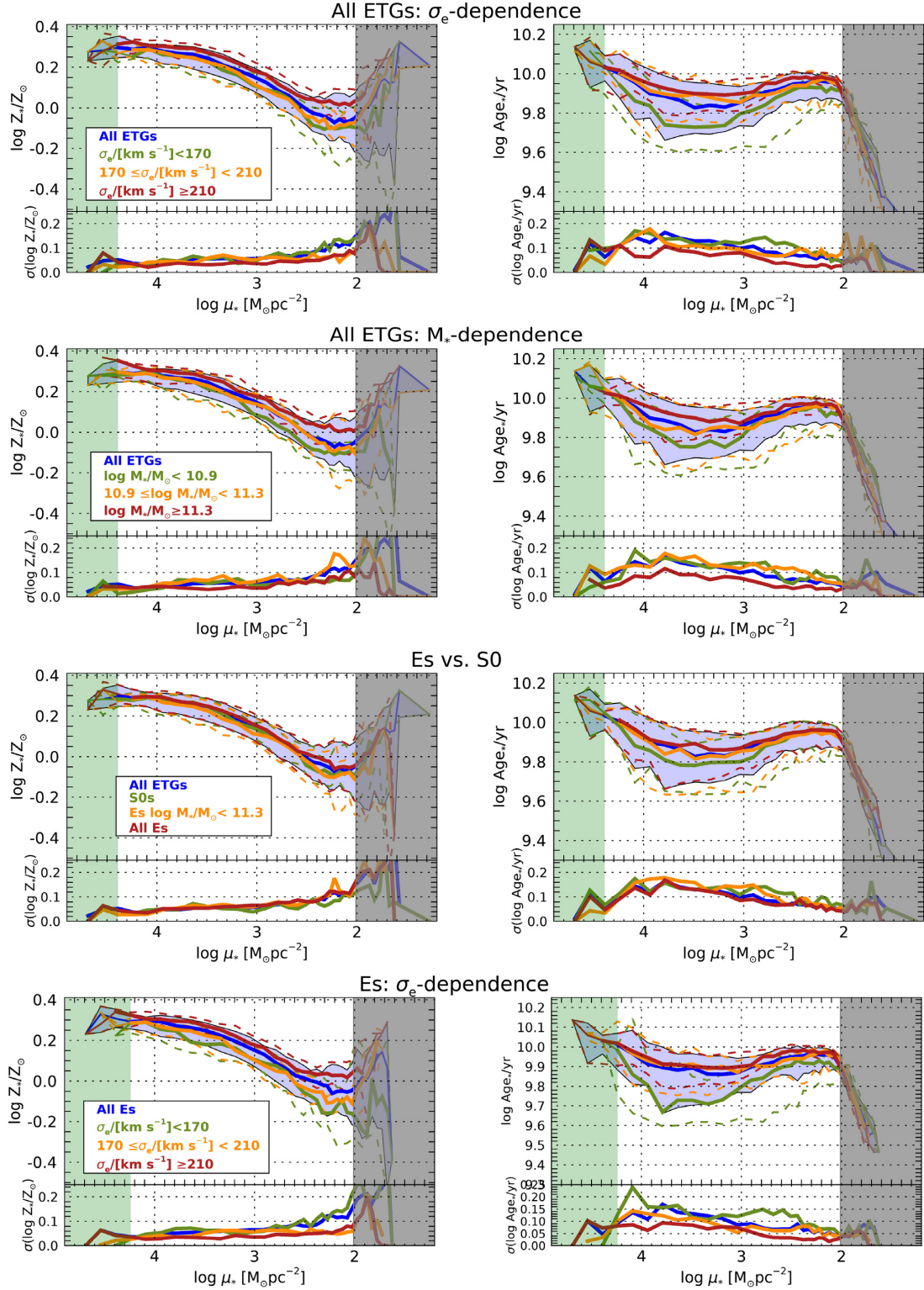
Figure 5. Profiles of light-weighted stellar metallicity Z_* (*left-hand column*) and stellar age Age$_*$ (*right-hand column*) as a function of $\log \mu_*$ for different galaxy subsamples. From the top row to the bottom: all ETGs binned according to their σ_e; all ETGs binned according to their M_*; Es versus S0 versus Es in the corresponding M_* range of S0; only Es binned according to their σ_e. The main panel of each plot displays the median profile of each bin (solid lines) and the 16th and 84th percentiles (dashed lines), colour-coded according to the legend. The blue line and shaded area correspond to the median and interpercentile range of the full unbinned sample (all ETGs for the first three rows, all Es only for the bottom row), and are reported for reference in all plots. The green-shaded regions indicate the range where less than 1/3 of the galaxies in the unbinned sample contribute. Line representing less than 1/3 of galaxies in a given subsample are thin. The grey-shaded regions mask the μ_* range where quantities are biased due to the surface brightness cut (see Section 4.2). In the bottom panels of each plot we report the scatter of individual profiles around the median of each subsample. *Most notably, a quasi-universal μ_*–Z_* relation emerges, whose zero-point is modulated by σ_e.*

$\sim 1.5\,R_e$, high-σ_e galaxies display almost flat profiles, with an inflection around $\sim 0.4\,R_e$; intermediate-σ_e galaxies reproduce very closely the median profile for the full sample and are characterized by a U-shape with a minimum of $\sim 6.8\,\mathrm{Gyr}$ at $\sim 0.4\,R_e$; finally, the low-σ_e galaxies display a monotonic age decrease towards the centre. Looking at the plots of scatter (both in Z_* and age) we note that the scatter in the σ_e subsamples is generally lower than in the full sample (except for the Z_* of low-σ_e galaxies at large radii). This is a further indication that σ_e alone induces clear systematic effects on the stellar population profiles.

In the second row of panels of Fig. 4 we plot the profiles in bins of M_*, including all ETG galaxies. We observe qualitatively very similar trends as with σ_e. We note minor differences in the metallicity profiles, whereby at SMA $< 1\,R_e$ the three mass bins overlap almost perfectly. The age profile of low-mass galaxies is more noisy than for the corresponding low-σ_e bin. Finally we note that the scatter in the bins is typically as large as in the general sample, except for the high-mass bin (which almost coincides with the high-σ_e bin). There is thus an indication that M_* has systematic effects on the profiles similar to σ_e, but the correlation is weaker and possibly inherited via the $\sigma_e - M_*$ correlation.

By comparing these binned profiles as a function of radius with the corresponding profiles as a function of stellar-mass surface density in Fig. 5, we observe that most of the profiles and relative trends are qualitatively consistent, after taking into account the different 'stretch' caused by the change of variable in abscissa. The visual impression is that different bins separate better, especially in Z_*, when profiles as a function of μ_* are used instead of radial profiles. We will better quantify this impression in the next Section 6.

We note that the Age$_* - \mu_*$ profile is U-shaped also for the low-σ_e subsample, contrary to the monotonically increasing behaviour observed in the corresponding radial profile. This is a consequence of the scatter in μ_* in the central regions and on its dependence on σ_e (see Fig. 3). As most of the low-σ_e galaxies do not reach μ_* as high as $10^{3.8}\,\mathrm{M_\odot\,pc^{-2}}$, the median inner *radial* profiles are dominated by the points at lower μ_*, hence at lower age. However, the top right-hand panel of Fig. 5 shows that even in low-σ_e galaxies there is a reversal of age gradients, provided that large enough densities are reached.

5.2 Profile dependence on E versus S0 morphology

In the third and fourth rows of plots in Figs 4 and 5 we investigate the impact of morphology on the stellar population profiles. The plots labelled 'Es versus S0s' in the third row of the two figures display the comparison between S0's (in green) and ellipticals (full sample, in red). We also plot the median profiles for ellipticals in the same mass range as S0's ($\log M_*/\mathrm{M_\odot} < 11.3$, in orange), in order to check to what extent differences in the profiles are induced by the different mass range spanned by the two morphological classes.

The median metallicity of S0's is systematically higher than the one in E's by $0.05 - 0.1\,\mathrm{dex}$ for a substantial part of the radial extent, between ~ 0.6 and $\sim 1.3 R_e$. Conversely, the median light-weighted age of the stellar populations in S0 galaxies is systematically lower than in E's by $0.05 - 0.1\,\mathrm{dex}$, over the same radial range. By restricting the comparison to E's matching the mass range of S0's, we observe qualitatively the same effects, although the difference is marginally smaller on average in Z_* and larger in age. This systematic variation between E's full sample and the mass-matched sub-sample stems from the trend with stellar mass observed in the second row of panels in Fig. 4.

Contrary to radial profiles, as a function of μ_*, the metallicity profiles of E's and S0's are hardly distinguishable, a fact that further stresses the fundamental nature of the relation between Z_* and μ_*, which is insensitive to the morphology of the galaxy.[4] In terms of their Age$_*(\mu_*)$ profiles, we observe systematic differences between E's and S0's, with the latter having younger minima by some 0.1 dex, even when compared to the mass-matched subsample of E's.

The fourth row of panels in Figs 4 and 5 repeat the same analysis of the respective top rows, i.e. the average profiles for different bins of σ_e, but now excluding S0's. We find indeed very similar profiles and trends. The most notable variations occur in the lowest-σ_e bin, whose difference relative to higher-σ_e bins appears amplified when S0's are excluded. In particular, the offset of the age profile of the low-σ_e bin to younger values with respect to the general sample is more significant when S0's are excluded from the analysis. A possible explanation for this might be that σ_e is a low-biased indicator of the dynamical support for S0's with respect to E's and therefore the binning in σ_e for the general sample produces more heterogeneous subsamples than for the pure E sample.

The morphological classification into E and S0 is nowadays often regarded as a primitive tool to separate 'pressure supported' from 'rotation supported' systems, despite the morphological classification having its own peculiarities that are not captured by a kinematic classification. A full characterization in terms of kinematics would allow us to properly separate the so-called 'slow rotators' from the 'fast rotators' (Emsellem et al. 2011). Unfortunately we have this characterization available only for the 54/69 galaxies in Falcón-Barroso et al. (2017), so we cannot perform a complete analysis here. However, from Falcón-Barroso, Lyubenova & van de Ven (2015) we can easily see that S0's are an almost pure sample of fast rotators, while Es are a mixed bag of fast rotators and slow rotators, with Es at $M_* > 10 \times 10^{11.3}\,\mathrm{M_\odot}$ being almost only slow rotators. So, already from the plots in Figs 4 and 5 we can infer that slow rotators tend to have flatter age profiles than fast rotators, which, in turn, present stronger age minimum and profile inflection at $\sim 0.4 R_e$. Massive slow rotators tend to slightly flatter radial profiles also in metallicity.

5.3 Characterization of profiles by reference values

In order to provide a more quantitative characterization of the profiles, for each galaxy we evaluate Age$_*$ and Z_* at different reference radial (SMA) distances and stellar surface mass densities (μ_*). We define the following set of reference radial distances:

   (i) 'centre' (SMA $< 0.1\,R_e$)
   (ii) $0.2\,R_e$ ($0.15 \leq \mathrm{SMA}/R_e < 0.25$)
   (iii) $0.4 R_e$ ($0.35 \leq \mathrm{SMA}/R_e < 0.45$)
   (iv) R_e ($0.95 \leq \mathrm{SMA}/R_e < 1.05$)
   (v) $2\,R_e$ ($1.95 \leq \mathrm{SMA}/R_e < 2.05$)

In brackets we report the discrete SMA ranges used to compute the characteristic stellar population parameters. We introduced the $0.2\,R_e$ distance because it is generally more robust both from a statistical point of view (more contributing spaxels) and from a observational/physical point of view (insensitive to residual PSF mismatches between photometry and IFS, and to possible nuclear

---

[4]The universality of $Z_*(\mu_*)$ on one hand and the dependence of $Z_*(\mathrm{SMA})$ on morphology on the other hand are a consequence of the stellar mass surface density profiles $\mu_*(\mathrm{SMA})$ changing systematically with the morphology.
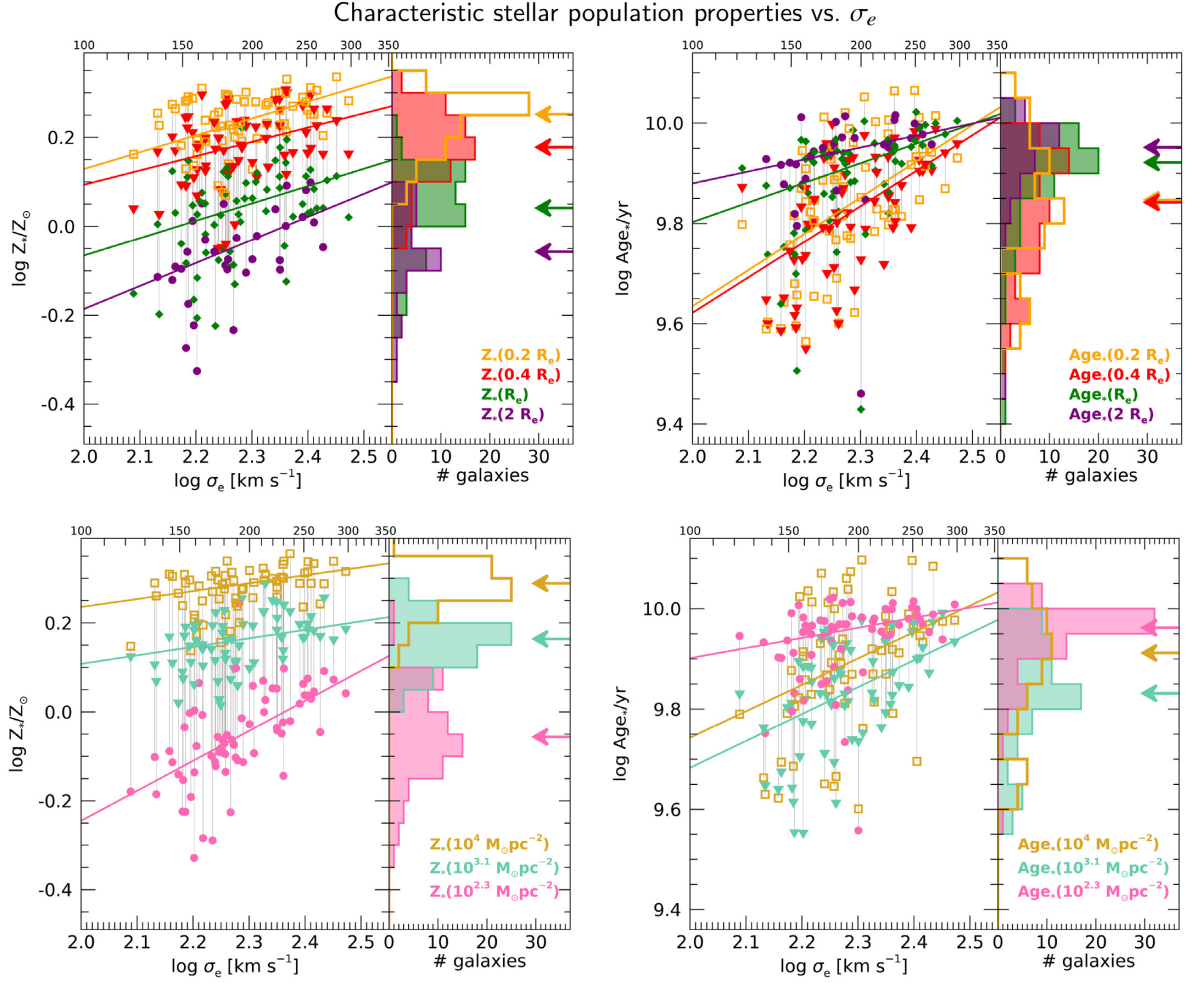
Figure 6. Characteristic stellar population properties (Z_*, *left-hand column*, and Age$_*$, *right-hand column*, respectively) are plotted as a function of the velocity dispersion within R_e, σ_e, in the main panel of each plot. The *right-hand side* panel displays the histogram of the distribution, with arrows marking the median. In the *top* row of plots stellar population properties are evaluated at some reference SMA in units of R_e, while in the *bottom* row they are evaluated at some reference μ_*. Different colours identify different reference SMA and μ_* (see the legends). Each thin vertical grey line connects points relative to the same galaxy. We plot in colour the robust linear regression lines obtained from a least absolute deviation algorithm. *Notably, all stellar population properties at characteristic SMA and μ_* are significantly and positively correlated with σ_e.*

sources, e.g. AGN) with respect to the 'centre' region, yet it is a fair representation of the innermost regions. The $0.4\,R_e$ reference is chosen as the approximate location of the age minimum. Similarly, we define a set of three reference stellar mass surface densities as follows:

(i) 'centre' ($\log \mu_* = 4.0$)
(ii) 'mid' ($\log \mu_* = 3.1$)
(iii) 'outer' ($\log \mu_* = 2.3$)

For each reference μ_*, the characteristic stellar population parameters are computed considering only the spaxels having μ_* within ± 0.1 dex from the reference. For each galaxy subsample, we compute the median and the 16th and 84th percentiles of the distribution of Age$_*$ and Z_* in the spaxels bins defined above, and report them in tables C1 and C2 (available online), in the form of median$^{+(p84-\text{median})}_{-(\text{median}-p16)}$, along with the number of contributing galaxies. The distributions of the characteristic stellar populations are represented in form of histograms in the right-hand side panels of Figs 6 (and 7, identical), where the median values are highlighted by arrows. These histograms and arrows clearly display the

systematic shape of the stellar population profiles described in this section.

6 TRENDS IN STELLAR POPULATION PROFILES WITH GLOBAL GALAXY PROPERTIES

In this section we further examine the dependence of stellar population profiles on global galaxy properties (e.g. M_*, σ_e, etc.), by studying the trends between these properties and Age$_*$ and Z_* evaluated at reference radial (SMA) distances and stellar surface mass densities (μ_*), as defined in the previous section.

In Fig. 6 we show how Z_* (left-hand column) and Age$_*$ (right-hand column), at different reference SMA (top row) and reference μ_* (bottom row), respectively, correlate with the stellar velocity dispersion σ_e. The main panel of each plot displays the points for individual galaxies in different colours for the different reference quantities. Points for the same galaxy are connected by vertical thin lines. The thick lines are obtained from robust linear regression via least absolute deviation minimization. The coefficients of the

Characteristic stellar population properties vs. M_*
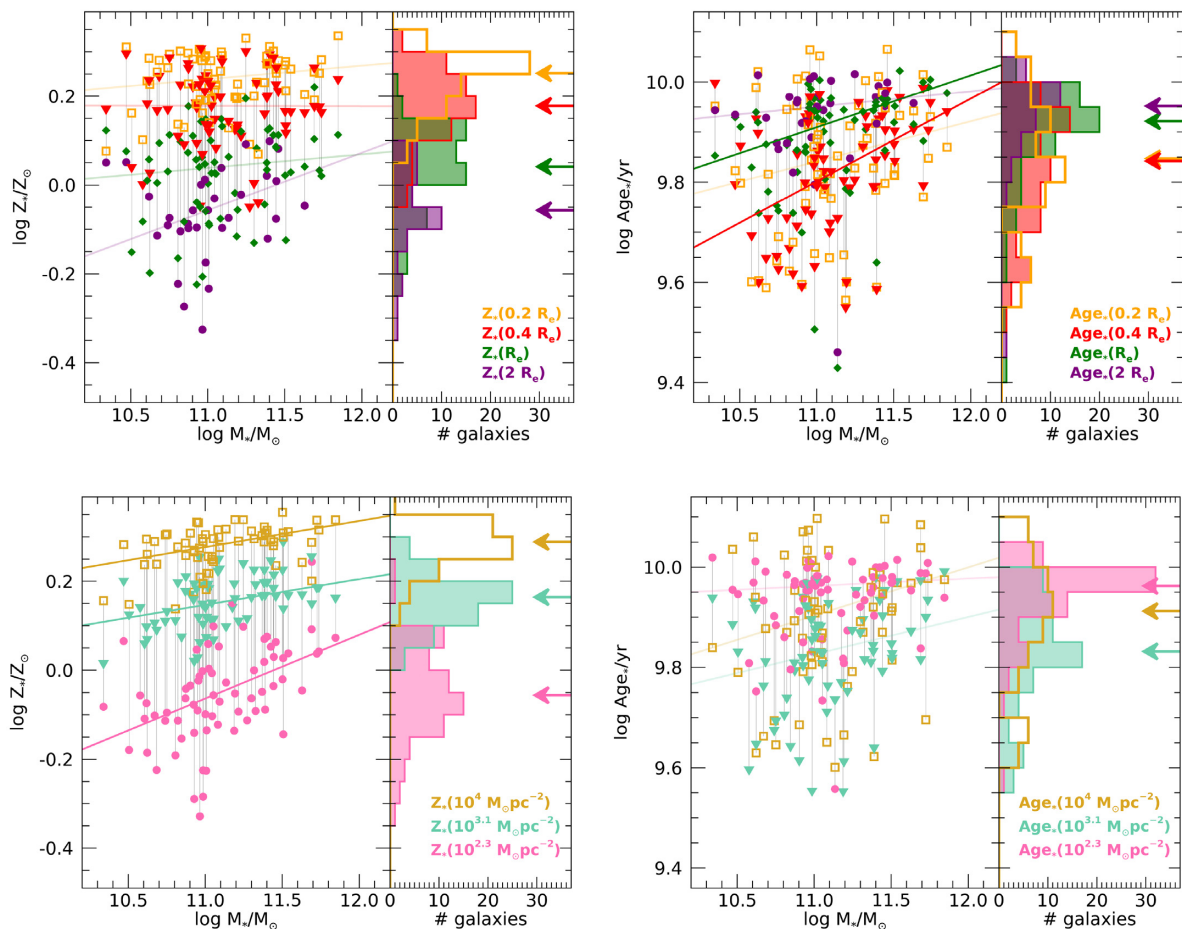
Figure 7. Characteristic stellar population properties (Z_*, *left-hand column*, and Age_*, *right-hand column*, respectively) are plotted as a function of the total stellar mass M_* in the main panel of each plot. The *right-hand side* panel displays the histogram of the distribution, with arrows marking the median. In the *top* row of plots stellar population properties are evaluated at some reference SMA in units of R_e, while in the *bottom* row they are evaluated at some reference μ_*. Different colours identify different reference SMA and μ_* (see legends). Each thin vertical line connects points relative to the same galaxy. We plot in colour the robust linear regression lines obtained from a least absolute deviation algorithm. Thin lines are used for correlations that are significant with a probability less than 99 per cent, according to the Spearman's rank correlation test. *While positive correlations with M_* are found for all quantities, they are weaker than those with σ_e and, in several cases, not statistically significant. This is an indication that M_* drives stellar population profile indirectly, through the correlation with σ_e.*

fits, the mean absolute deviation (MAD), the Spearman's rank correlation coefficient $C_{Spearman}$, and the resulting probability for null correlation P_{null} are reported in columns 5 to 9 of tables C3 and C4 (available online). The right-hand side panels of the plots display the number distribution in Z_* and Age_* for the different reference quantities. Arrows mark the position of the median of the distributions (see also tables C1 and C2, available online).

All characteristic stellar population properties are positively correlated with σ_e, at > 99 per cent confidence level, according to a simple Spearman's rank correlation test. In other words, at any radius or stellar mass surface density we find a trend for both Z_* and Age_* to increase at increasing velocity dispersion.

The trends of metallicities at different reference SMA (Fig. 6, top left-hand panel) have all a very similar slope, thus implying that the effect of σ_e on the radial metallicity profiles is essentially a vertical shift, by about 0.04 dex per 0.1 dex in σ_e, corresponding to about 0.15 dex over the σ_e range spanned by our sample. The only exception occurs in the very centre ('centre' region, only reported

in the tables, not shown in the plots), where all profiles appear to converge. There we measure a weaker correlation with σ_e and all galaxies share the same estimated $\log Z_*/Z_\odot \sim 0.3$ within a few 0.01 dex. Note that this central convergence may be partly an effect of saturation towards the highest metallicity allowed in the spectral library.

At fixed μ_*, the trends of Z_* with σ_e (Fig. 6, bottom left-hand panel) are flatter than at fixed SMA in the high and intermediate density regions, but significantly steeper in the low density regions, with an increase of ~ 0.07 dex in metallicity per 0.1 dex in σ_e. This is a quite remarkable effect as one would naively expect that σ_e (which traces the dynamics in the densest regions) would affect mostly the densest regions of the galaxies. What we see, instead, is a correlation between the inner dynamical state (possibly a tracer of the depth of the gravitational potential well) with the metallicity of the low density regions, which simulations indicate being composed by a significant fraction of stars accreted from satellites (e.g. Hirschmann et al. 2015; Rodriguez-Gomez et al.

2016). This, in turn, highlights a strong link between halo mass (whose σ_e is a proxy) and the surrounding environment in terms of the properties of stellar populations of its satellite galaxies.

Characteristic ages show steeper positive trends with σ_e for the inner reference radii ($0.4, 0.2\,R_e$) than for the outer ones (1 and $2\,R_e$). This is consistent with σ_e driving the scatter in the radial profiles of Age$_*$ and with the substantial decrease of the galaxy-to-galaxy scatter as one moves outwards. Going from ~ 130 to $\sim 300\,\mathrm{km\,s^{-1}}$ galaxies roughly double their age in the inner $\sim 0.5\,R_e$, but increase their age by ~ 25 per cent only beyond $1\,R_e$. From the convergence of the different trend lines we also see that age profiles become essentially flat for $\sigma_e \gtrsim 300\,\mathrm{km\,s^{-1}}$. The trends of characteristic Age$_*$ at different μ_* (bottom-right plot of Fig. 6) confirm this picture by displaying flat slopes at low μ_* and steeper slopes at higher μ_*, with a substantial convergence at $\sim 300\,\mathrm{km\,s^{-1}}$. We can summarize these trends by saying that high-σ_e ETGs are homogeneously and maximally old, while at lower σ_e they become increasingly younger, more so in the inner $\sim 0.5\,R_e$.

In Fig. 7 we repeat the analysis of Fig. 6, but considering the stellar mass M_* as the variable against which to check for trends, instead of σ_e. In this figure, regression lines are drawn as thick or thin lines depending on whether the hypothesis of null correlation can be excluded with a probability of more of 99 per cent or less, respectively. Although qualitatively we obtain similar trends of characteristic Z_* and Age$_*$ increasing with M_*, as opposed to the correlations with σ_e (all significant), only 6/14 correlations with M_* are significant. This can be understood if we interpret the correlations with σ_e as 'primary' correlations and the ones with M_* as second order correlations, 'inherited' from the correlation between M_* and σ_e (see Fig. 1). In particular, we note that none of the correlations with Z_* at fixed radii retains its significance, whereas correlations with Z_* at fixed μ_* do. This is further indication of the fundamental role of μ_*, rather than radial distance, in determining the metallicity of the stars in an ETG.

Significant age trends with M_* are only observed at $0.4\,R_e$ and $1\,R_e$. Those are also the most significant trends against σ_e (see table C1, available online) and this observation confirms the hypothesis that correlations with M_* are actually second order correlations, 'inherited' from the correlation between M_* and σ_e.

We further explore possible correlations of the shape of the stellar population profiles with the 'global' parameters represented by the metallicity and the age evaluated at $1\,R_e$, $Z_*(R_e)$ and Age$_*(R_e)$, and with different concentration indices for the light distribution. The choice of $Z_*(R_e)$ and Age$_*(R_e)$ as global parameters is justified because they can be considered as reasonable proxies for the galaxy-integrated stellar metallicity and age, respectively (see also González Delgado et al. 2015). From tables C3 and C4 (available online) we note that most correlations of $Z_*(R_e)$ and Age$_*(R_e)$ are with characteristic Z_* and Age$_*$, respectively. These correlations are partly built-in, given the continuity of the profiles. However, they also indicate that changes in the profile shapes, if any, correlate with their normalization at $1\,R_e$.

We also note some weak or marginally significant positive correlations between characteristic Z_* and Age$_*(R_e)$. Vice versa, we observe some tentative positive correlations between characteristic Age$_*$ and $Z_*(R_e)$, although they are milder and much less significant ($P_{\mathrm{null}} \gtrsim 0.1$). We interpret these correlations as second order effects, deriving from the primary correlations with σ_e. Interestingly, there is virtually no correlation between $Z_*(R_e)$ and Age$_*(R_e)$.

Finally, we do not observe any significant correlation between characteristic stellar population parameters and concentration index of the light profiles. In tables C1 and C2 (available online) for

illustration we only report on the correlation analysis with the C_{31} index, which is defined as the ratio between the radii enclosing 75 per cent and 25 per cent of the total light, R_{75} and R_{50}, respectively. We get consistent results also for other concentration indices, namely for $C_{95} \equiv \frac{R_{90}}{R_{50}}$ and for $C_{21} \equiv \frac{R_{50}}{R_{25}}$, which are sensitive in different degrees to different parts of the profile, although obviously correlated (and equivalent in case of ideal Sérsic profiles). This lack of measurable correlation may partly arise from the small dynamic range of the concentration parameters in our sample. In fact, Zhuang et al. (2019) analysed the stellar metallicity profiles for a sample of CALIFA galaxies spanning the full morphological range and found a clear dependence of the radial metallicity profile on the Sérsic index.

7 STELLAR POPULATION GRADIENTS AND THEIR TRENDS WITH GLOBAL PROPERTIES

In this section we provide some more quantitative estimates on the shape of the stellar population profiles that can be useful for comparison with other observations and with models (e.g. Hirschmann, in preparation).

7.1 Radial stellar population gradients

We quantify the radial variations of stellar population properties inside ETGs by means of linear and logarithmic radial gradients that we define as:

$$\nabla_{\mathrm{lin}} X \equiv \frac{\partial \log X}{\partial \mathrm{SMA}} \tag{3}$$

$$\nabla_{\mathrm{log}} X \equiv \frac{\partial \log X}{\partial \log \mathrm{SMA}}, \tag{4}$$

respectively, where X is either Z_* or Age$_*$. Inspite of the ill-defined nature of a global gradient for profiles that are neither pure exponential nor power-law, as we showed in the previous sections, this kind of profile characterization is quite common in the literature (e.g. Kuntschner et al. 2010; Martín-Navarro et al. 2018) and may be helpful for comparison purposes and to compress the information. Considering the 'curvature' of the profiles we define the radial gradients over two distinct ranges: an inner range from $0.2\,R_e$ to $1\,R_e$, and an outer range from $1\,R_e$ to $2\,R_e$. We exclude the very inner region to avoid biases in the estimate due to low-number of spaxel statistics and PSF smearing effects. For each galaxy, the gradient values are computed as the ratio of finite differences between the values at the boundaries of the ranges. In particular, in these differences we consider Z_* and Age$_*$, respectively, evaluated as the median in the spaxels within 0.1–R_e-wide annuli centred at the respective boundaries of the ranges. In table D1 (available online) we report the values of the radial (linear and logarithmic) gradients for the different galaxy subsamples, both for the inner and the outer regions. The reference value in each column is the median of the sample, the plus-minus values represent the 16th − 84th percentile range.

Metallicity gradients are all negative but in two cases, where we measure slightly positive inner gradients (indeed very close to flat). We observe a flattening from inner to outer gradients in linear scale, and vice versa in logarithmic scale. This is consistent with the profiles observed in Figs 2 and 4 and with the different stretch when logarithmic radial scale is used instead of linear. The significance of this effect is evident from the histograms in the side-panel of the top left-hand plot of Fig. 8. These distributions are clearly inconsistent with constant-slope profiles at more than
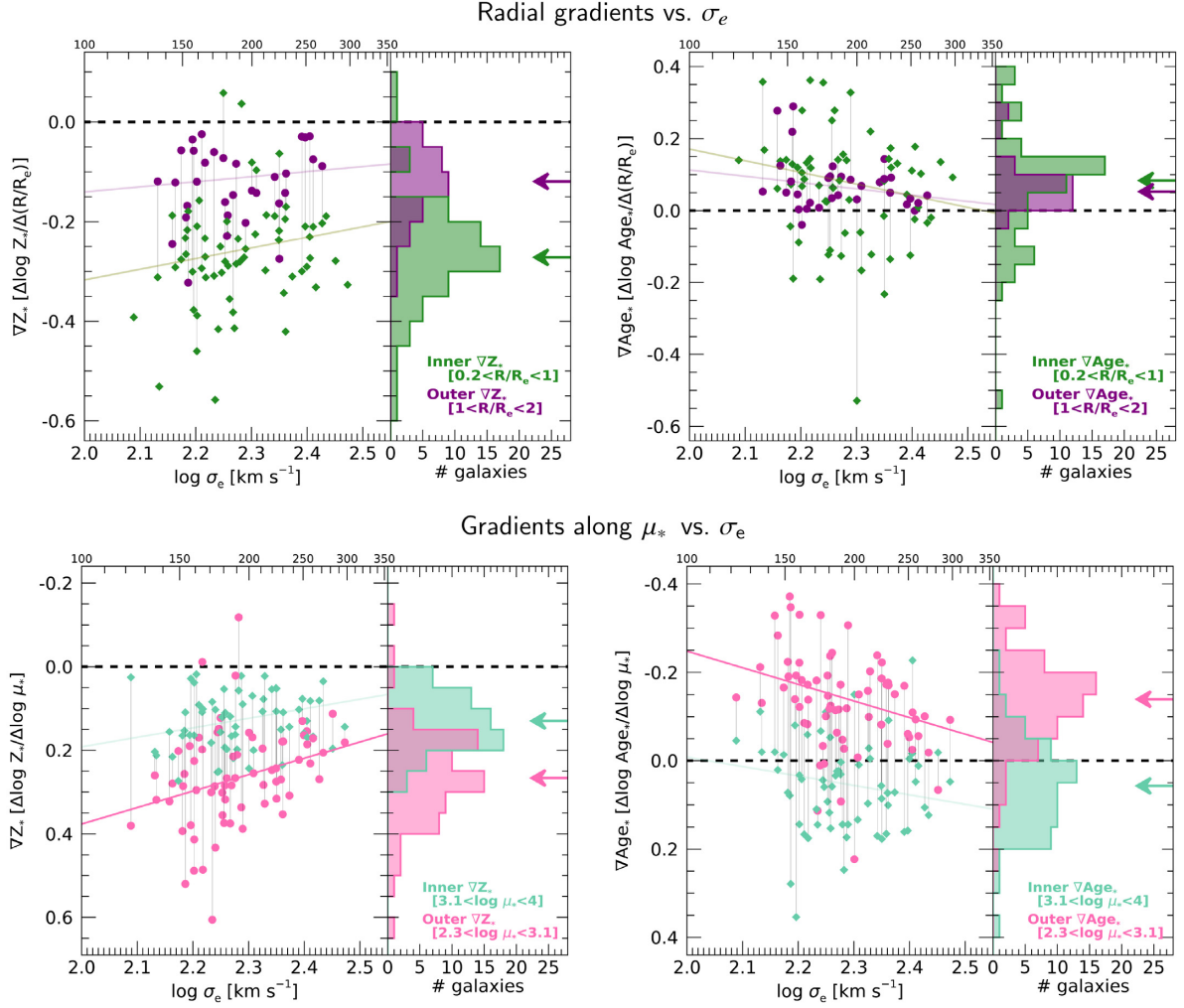
Figure 8. Dependence of various stellar population gradients on the velocity dispersion σ_e. Radial gradients are displayed in the *top row*, gradients along μ_* in the *bottom row*; Z_* gradients are presented in the *left-hand column* plots, Age$_*$ gradients in the *right-hand column*. The main panel of each plot reports the points for individual galaxies, with different colours for the different ranges of SMA or μ_* (see legends). Points relative to the same galaxy are connected with vertical thin lines. Lines in colour represent the robust fit to the data; a thin transparent style is used when the correlation is deemed as not significant (see the text). The side panels to the *right* of the main ones display the histograms of the gradient values. Arrows mark the median of the distributions. Note that the y-axis for the gradients along μ_* is reversed, so to ease the comparison with radial gradients, whereby points below the zero line (dashed horizontal line) indicate trends of decreasing property going from the centre towards the outskirts.

3σ significance. From table D1 (available online), we see very little variations among the different samples. The inner gradients in the various subsamples depart from the median inner gradient of the full sample ($-0.27\,\text{dex}\,\text{R}_e^{-1}$ or $-0.31\,\text{dex}\,\text{dex}^{-1}$) by no more than $0.04\,\text{dex}\,\text{R}_e^{-1}$ (or $0.05\,\text{dex}\,\text{dex}^{-1}$), which is half of the overall galaxy-to-galaxy scatter. If anything, the most massive or high-σ_e galaxies tend to have slightly flatter inner Z_* profiles than average. A similar hint is seen also in the outer gradients. However, as we will show in Section 7.3, these trends are not statistically significant.

Inner age gradients are on average positive, with a typical increase of $20-25$ per cent per R_e between the inner $0.2\,R_e$ and $1\,R_e$. The scatter, however, is large, so that 19/65 galaxies (29 per cent) have measured negative gradients. This results from the diverse U-shapes observed in the age profiles within $1\,R_e$. We just note a marginal indication for low-σ_e galaxies to display steeper positive age gradients, which is consistent with the top right plot of Fig. 2 As already observed in the previous sections, the age profiles become

less scattered beyond $1\,R_e$, where we still observe mildly positive gradients but with a much less scattered distribution.

7.2 Stellar population gradients along μ_*

Similar to radial gradients, in order to quantify the slopes of the variations of stellar population properties as a function of μ_*, we introduce the quantity ('gradient along μ_*'):

$$\nabla_{\mu_*} X \equiv \frac{\partial \log X}{\partial \log \mu_*}, \tag{5}$$

where X is either Z_* or Age$_*$. Also in this case, we define an inner range including the spaxels with high stellar mass surface density $3.1 < \log \frac{\mu_*}{\text{M}_\odot\,\text{pc}^{-2}} < 4$, and an outer range with $2.3 < \log \frac{\mu_*}{\text{M}_\odot\,\text{pc}^{-2}} < 3.1$. The break point between the two regimes is arbitrary located visually close to the inflection point in the median age profile in Fig. 2 (bottom right plot). ∇_{μ_*} gradients are obtained as the ratios of finite difference between the extremes of the range and

by adopting as $Z_*(\mu_*)$ and $\mathrm{Age}_*(\mu_*)$ the median Z_* and median Age_*, respectively, in all spaxels with surface mass density within $\log \mu_* - 0.1$ and $\log \mu_* + 0.1$. The values for the ∇_{μ_*} gradients for different subsamples are reported in table D2 (available online) . The reference value is the median over each (sub)sample and the plus–minus values correspond to the 84th and the 16th percentile of the distribution, respectively. The distributions of gradient values are also represented in the form of histograms in the side panels of the plots in the bottom row of Fig. 8. Given the monotonically decreasing nature of $\mu_*(\mathrm{SMA})$ profiles, positive ∇_{μ_*} gradients correspond to negative radial gradients, and vice versa. For this reason, in the bottom panels of Fig. 8 the vertical axis is flipped (positive to negative) compared to the top panels (negative to positive), in order to ease the visual comparison with the distribution of radial gradients.

Concerning metallicity gradients, we observe very similar distributions as for the radial case. Both inner and outer $\nabla_{\mu_*}(Z_*)$ distribute in the positive range of values (i.e. decreasing Z_* going to lower μ_*), with just a couple of exceptions. The gradients are flatter in the high μ_* regime and steeper at low μ_*, as already noted in Section 4 and from Fig. 2. The galaxies in the highest mass bin and in the highest σ_e tend to have flatter inner gradients, although the significance of the effect is rather low.

Concerning age gradients, inner gradients present a broad distribution around 0, with a slightly positive median of 0.06 dex per dex (i.e. decreasing Age_* going to lower μ_*). This distribution is the consequence of the inner range embracing the region around the age dip, with a net effect of an overall flat profile. The distribution of outer age gradients is instead well defined negative (i.e. increasing Age_* going to lower μ_*), with just a minor tail of galaxies extending towards 0 and positive values. A trend for steeper slopes at smaller masses and σ_e is also apparent.

7.3 Dependence of gradients on global properties

In this section we investigate possible dependencies of stellar population gradients on global quantities, in a similar way as we did in Section 6 for stellar population properties at fixed characteristic SMA or μ_*. In this way we can isolate variations in the shape of the profiles from the changes in the overall normalization.

We start off analysing the dependence of gradients on the stellar velocity dispersion σ_e, in Fig. 8. The main panels in these plots display the gradients (radial in the top row and along μ_* in the bottom row) of metallicity (left-hand column) and of age (right-hand column) as a function of σ_e, in various colours for different ranges, as indicated in the legends. We performed robust linear regression via least absolute deviation minimization. The results are displayed by the lines in different colours, matching the colour of the points. In tables D3 and D4 (available online) the coefficients of the fits, the mean absolute deviation (MAD), the Spearman's rank correlation coefficient C_{Spearman}, and the resulting probability for null correlation P_{null} are reported in the last five columns, respectively. If $P_{\mathrm{null}} < 0.01$ we deem the correlation as significant: the corresponding row in the table is checked, and the regression line is drawn with thick line; vice versa, the regression is shown with a thin transparent line.

Although we note general trends for profiles to become flatter as σ_e increases, we find significant statistical correlations only between σ_e and outer gradients along μ_*, both in metallicity and in age. If we take this result together with the ubiquitous significant correlations that we found between properties at fixed characteristic SMA and μ_* (see Fig. 6), we can conclude that σ_e drives systematic variations

in the stellar population profiles, although these variations do not affect the *shape* of the profiles chiefly, rather their *normalization*. In other words, by increasing σ_e from 120 to 300 km s^{-1} we mainly shift age and metallicity profiles to higher values, and in second place we produce flatter profiles. Note, however, that the gradients, as actually defined, do not capture the age dip around $0.4\,R_e$, which is strongly correlated with σ_e.

We repeat the correlation analysis of gradients against total stellar mass M_*, instead of σ_e, and report the results in tables D3 and D4 (available online) . Despite some very marginal indications for analogous trends as with σ_e, none of them is significant at more than 90 per cent level. This is yet another evidence that σ_e is the main driver of systematic changes in stellar population profiles and correlations with M_* are just inherited via the correlation between σ_e and M_*.

We also investigate possible correlations between various gradients and the metallicity and age evaluated at the effective radius, as representative of the global metallicity and age of the galaxy. The results are reported in tables D3 and D4 (available online) and the main correlations are plotted in Figs 9–11.

The strength of age gradients in the outer parts display anticorrelation trends with age at $1\,R_e$. These trends mainly result from the ages in the outer parts of galaxies being very uniform, so that the variations in gradients essentially depend on variations in $\mathrm{Age}_*(R_e)$. The larger scatter in the innermost regions results in non-significant correlations of the inner gradients with $\mathrm{Age}_*(R_e)$. This can be seen in two panels of Fig. 9, for gradients in radial direction and in μ_* (left-hand and right-hand panels, respectively). Note that the trends are not driven nor made more significant by the two galaxies with significantly lower $\mathrm{Age}_*(R_e)$, as we verified by repeating the analysis with those galaxies excluded.

Age gradients do not display any strong correlation with $Z_*(R_e)$. A marginally significant ($P_{\mathrm{null}} < 0.01$) anticorrelation is measured between the inner radial gradient of Age_* and $Z_*(R_e)$, whereby more metal-rich galaxies tend to have flatter gradients. The slope of this relation, however, is quite flat and results in a dynamic range for the gradients that is smaller than the scatter around the median value.

As a function of the metallicity at $1\,R_e$, $Z_*(R_e)$, we notice a significant trend of the inner radial metallicity gradients to become shallower as $Z_*(R_e)$ increases, as shown in Fig. 10. However, this trend is not seen for radial gradients relative to the outer regions. This is consistent with the *central* metallicity being roughly uniform while the scatter among the profiles keeps increasing while moving outwards up to approximately $1\,R_e$ (see Fig. 6 top left-hand panel and, e.g. Fig. 2 top left-hand panel). Trends with $Z_*(R_e)$ for metallicity gradients along μ_* are very mild, although a marginally significant trend for outer gradients becoming flatter at larger $Z_*(R_e)$ is measured.

In Fig. 11 we see that radial metallicity gradients beyond $1\,R_e$ correlate with $\mathrm{Age}_*(R_e)$, going from ~ -0.3 dex R_e^{-1} for the youngest ETGs to almost 0 (flat) for the oldest ones. This might indicate that metallicity gradients tend to be suppressed as galaxies age, possibly due to internal mixing processes or to external accretion events that mostly affect the outer regions. On the other hand, neither inner radial metallicity gradients nor metallicity gradients along μ_* display any significant correlation with age. This lack of strong trends for gradients along of μ_* can be due to the quasi-universal shape for the profiles of $Z_*(\mu_*)$, with just a second order dependence on σ_e in the outer parts (see previous section and Fig. 6 bottom left-hand panel). The aforementioned mixing mechanisms or accretion events should affect μ_* and Z_* in a way that, somehow, preserves

Age gradients vs. *Age(R_e)*
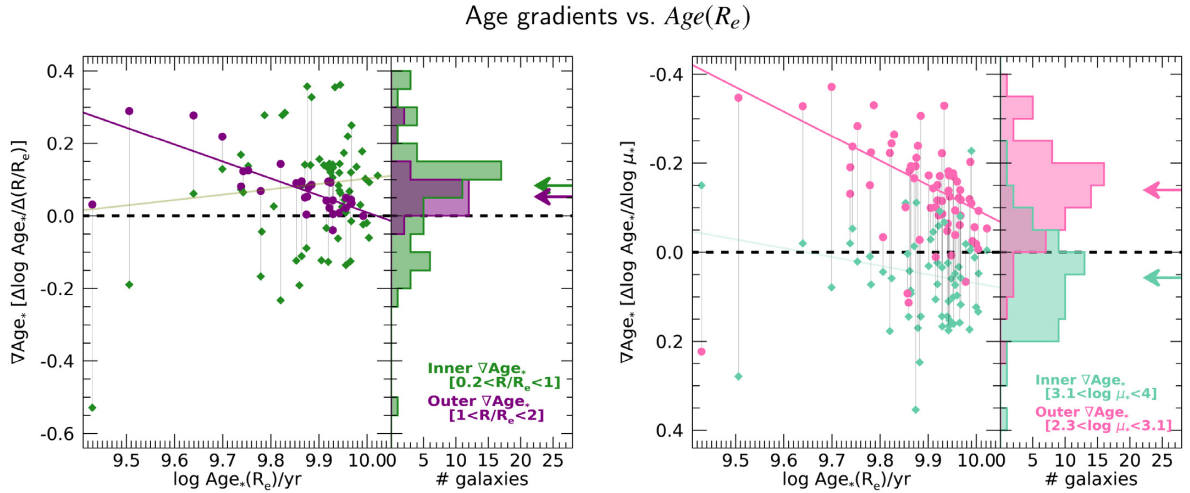
Figure 9. Dependence of various age gradients on the characteristic age at the effective radius, $\text{Age}_*(R_e)$. Radial gradients are displayed in the *left-side* plot, gradients along μ_* in the *right-side* one. The main panel of each plot reports the points for individual galaxies, with different colours for the different ranges of SMA or μ_* (see legends). Points relative to the same galaxy are connected with vertical thin lines. Lines in colour represent the robust fit to the data; a thin transparent style is used when the correlation is deemed as not significant (see the text). The side panels to the *right* of the main ones display the histograms of the gradient values. Arrows mark the median of the distributions. Note that the *y*-axis for the gradients along μ_* is reversed, so to ease the comparison with radial gradients, whereby points below the zero line (dashed horizontal line) indicate trends of decreasing Age_* going from the centre towards the outskirts.

Metallicity gradients vs. $Z_*(R_e)$
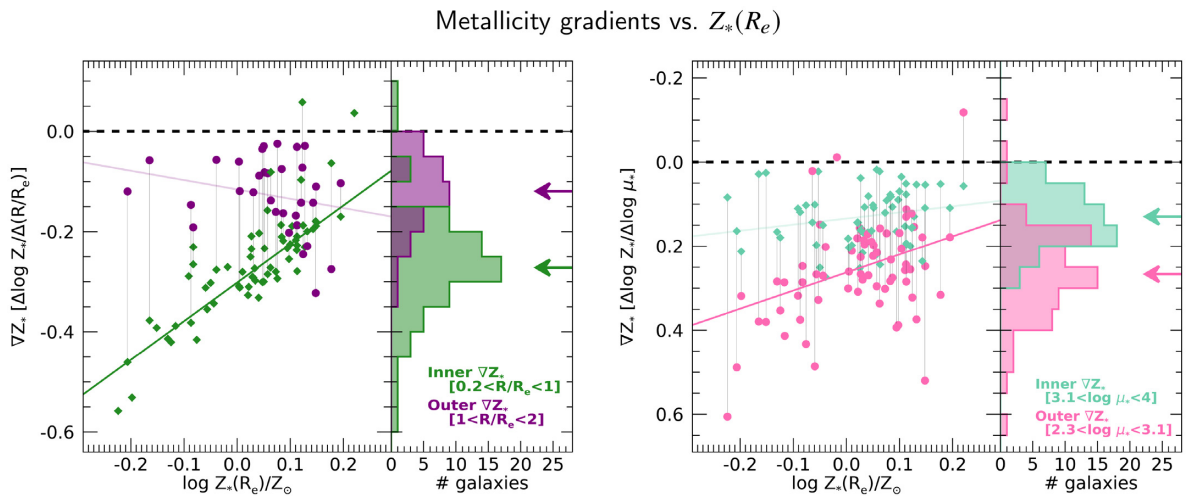
Figure 10. Dependence of various Z_* gradients on the characteristic Z_* at the effective radius, $Z_*(R_e)$. Radial gradients are displayed in the *left-side* plot, gradients along μ_* in the *right-side* one. The main panel of each plot reports the points for individual galaxies, with different colours for the different ranges of SMA or μ_* (see legends). Points relative to the same galaxy are connected with vertical thin lines. Lines in colour represent the robust fit to the data; a thin transparent style is used when the correlation is deemed as not significant (see the text). The side panels to the *right* of the main ones display the histograms of the gradient values. Arrows mark the median of the distributions. Note that the *y*-axis for the gradients along μ_* is reversed, so to ease the comparison with radial gradients, whereby points above the zero line (dashed horizontal line) indicate trends of increasing Z_* going from the centre towards the outskirts.

the $Z_*(\mu_*)$ relation while suppressing the radial Z_* gradients, i.e. produce a slowly decreasing mass surface density profiles along with a mild radial decrease in metallicity.

Finally, we looked for possible correlations between stellar population gradients and light concentration indices (see end of Section 6), but found none. As already noted, the range in concentration indices in our sample of (massive) ETGs is too small to make a statistically significant detection of correlations possible with a relatively small data set like ours. However, based on the results by Zhuang et al. (2019), it is tantalizing to think that stellar population gradients may actually depend on the light concentration index over a broader range, thus covering not only ETGs but also late type galaxies.

As a general conclusion, we can state that *whenever a trend is visible (even if the statistical significance is low), it goes in the direction of older/more metal-rich/more massive/higher velocity-dispersion galaxies having flatter gradients*.

8 DISCUSSION

Stellar population profiles and gradients in ETGs have been the subject of extensive studies in the last decades, both observationally and theoretically. As already pointed out in the Introduction, the attention to this topic is justified by the fundamental constraints that stellar population profiles can provide in order to discriminate between different scenarios of formation and evolution of ETGs. In

Metallicity gradients vs. $Age_*(R_e)$
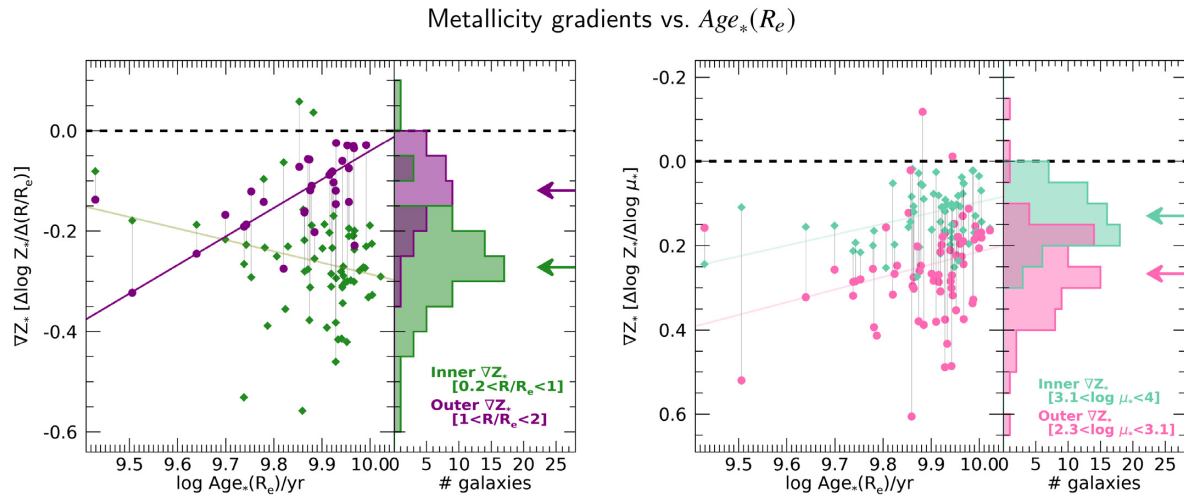
Figure 11. Dependence of various Z_* gradients on the characteristic Age_* at the effective radius, $Age_*(R_e)$. Symbols and lines as in Fig. 10.

this section we discuss how our results position themselves in this context and suggest a possible evolutionary scenario for the ETGs that can explain our observations.

8.1 Stellar population profiles: state of observations

From an observational point of view, we can compare our results with various analyses of long-slit or integral field spectroscopic observations, which mainly focus on radial profiles rather than on their dependence on μ_* (with the notable exception of González Delgado et al. 2014, see below).

Age and metallicity estimates in the literature are based on a very diverse set of methods (absorption indices, full spectral fitting, photometry) and assumptions regarding the models. Popular 'fitting' methods are based on different philosophies. Concerning the observational data, methods that focus on absorption indices (and colours) privilege the reliability of the models predictions over a limited set of features and wavelengths and the robustness of the measurements, while full spectral fitting methods privilege the statistical power given by the large number of pixel wavelengths at the expenses of possible model mismatches and flux calibration biases. Differences are also found in the statistical approach, ranging from frequentist to Bayesian, from parametric to fully non-parametric.

Concerning the models, there is a huge spectrum of approaches. Comparing with simple stellar population (SSP) models is still very popular for ETGs, despite their SFH not being for sure a single burst of single metallicity. Among approaches based on composite stellar populations, choices range from single parametric SFH, to parametric plus stochastic SFH, to fully non-parametric SFH. Dust attenuation is also treated very differently by various authors: in some works it is assumed to be negligible and is not modelled, in others it is treated in screen approximation, in others (like in this work) it is implemented in a mixed star-dust geometry.

How these model assumptions affect (or possibly bias) estimates of ages and metallicity depend also on the statistical method adopted. We stress that one of the key advantages of our Bayesian method is to consider the full PDF of the physical quantities, over the broadest range of theoretical models, therefore to account for complexity and intrinsic model degeneracy. Last but not least, different works are based on different basic stellar population

synthesis ingredients, such as evolutionary tracks, isochrones, and spectral libraries.

As a consequence, a direct comparison between different works, especially in quantitative terms, is often all but straightforward. A comprehensive review of all these studies and of the reasons of their (dis)agreement is beyond the scope of this paper. It is interesting, however, to highlight the points that persist among the different studies (and therefore can be considered 'robust') and the novelties of our analysis and results. In the following discussion we will consider only results for ETGs in the velocity dispersion range covered by our present work, $100 \lesssim \sigma/[\mathrm{km\,s^{-1}}] \lesssim 300$, or equivalently in the stellar mass range above $\sim 10^{10.3}\,\mathrm{M_\odot}$.

8.1.1 Radial metallicity gradients

Most past works in the literature agree on the presence of negative metallicity gradients within $1\,R_e$, whose amplitude varies from -0.3 dex per R_e (or equivalently -0.3 dex per dex in radius) to ~ -0.1, hence broadly consistent with our findings. It is worth noting that different authors adopt different methods to measure gradients. Some authors work with linear radial scale, some other with logarithmic radial scale (we report both). Some measure the gradients via linear regression, while some others (including us) estimate the gradient via discrete difference ratio.

Mehlert et al. (2003) analysed a sample of 35 ETGs (both E and S0) in the Coma cluster with long-slit spectroscopic observations that allowed for a minimum spatial coverage of $1\,R_e$. Based on stellar absorption indices and SSP predictions, they estimate typical central metallicity values of [Z/H] ~ 0.2 and logarithmic radial gradients within $1\,R_e$ of -0.16 dex per dex, with an rms of $\sim 0.10 - 0.15$. A consistent result was found by Spolaor et al. (2009) using a compilation of their own data and results from Brough et al. (2007), Reda et al. (2007), Sánchez-Blázquez et al. (2007): their logarithmic radial gradients of metallicity are in the range 0 to -0.5, with a clear trend for flatter profiles at larger velocity dispersions, provided that the brightest cluster/group galaxies are excluded.

Kuntschner et al. (2010) analyse a sample of 48 ETGs as part of the IFS survey SAURON, also based on stellar absorption indices interpreted both with SSP models and with composite stellar populations according to their reconstructed SFH. They obtain consistent results with the two approaches and found typical

central metallicities of [Z/H] ~ 0.1 and logarithmic radial gradients within 1 R_e of ~ -0.3, very similar to our estimates. In their fig. 14 one can also note a tentative trend for metallicity gradients to get shallower as σ_e increases. A very similar result was found by Koleva et al. ([2011](#)) based on a sample of 40 ETGs observed in long-slit spectroscopy. Steep negative metallicity gradients, similar to those found in the works listed so far, can be inferred from the aperture-integrated measurements published by McDermid et al. ([2015](#)) based on ATLAS^{3D} data.

Stellar population gradients have been derived for large samples of ETGs ($N \gg 100$) in the IFS survey MaNGA, based on different inference methods. Goddard et al. ([2017](#)) adopted a full-spectrum fitting approach based on the FIREFLY code (see references in their paper) and found typically mild logarithmic gradients in metallicity, both light- and mass-weighted, in the range -0.13 to -0.06, which is slightly shallower than our measurements. The generally poorer physical spatial resolution in MaNGA than in CALIFA (typically a factor 2 to 4 worse, depending on the bundle employed in MaNGA), may explain part of this difference, as measured profiles appear shallower than in reality, as shown by the simulations by Ibarra-Medel et al. ([2019](#)). Interestingly, by mass-weighing they measure marginally flatter gradients than by light-weighing. Considering the typical temporal evolution of M/L, which increases with time, and the almost perfect correspondence between light- and mass-weighted metallicity in the centre, this effect suggests that at $R \gtrsim 1 R_e$ the metallicity decreases in the youngest stars, contrary to expectations from a scenario of self-enrichment. In turn, this can be interpreted as a sign of ex-situ accreted stars or stars formed from external metal-poor gas. Indeed, the accretion of a metal-poor stellar envelope is also invoked by Oyarzún et al. ([2019](#)) to explain the flattening of the outer metallicity profile that they observe in the most massive ETGs in MaNGA, based on a simple prescription derived from the Illustris simulation (D'Souza & Bell [2018](#)). While the strength of the metallicity gradient is almost unchanged in different mass bins, Goddard et al. ([2017](#)) show a significant overall offset of ~ 0.1 dex in the two top mass bins ($10.55 < \log M_*/M_\odot < 11.05$ and $\log M_*/M_\odot > 11.05$). We recall that we find a similar trend with σ_e, while our trend with M_* is small and not statistically significant.

Li et al. ([2018](#)) performed full-spectrum fitting analysis on a sample of ~ 2000 galaxies in MaNGA, including 952 ETGs, by using PPXF to estimate light-weighted ages and metallicity. They found negative metallicity gradients for the vast majority of massive / high-σ_e ETGs, with logarithmic slopes in the range $-0.25 - \sim 0$, with a median of ~ -0.1. These gradients are somewhat shallower than what we measure, however part of the disagreement might be due to their poorer spatial resolution, and part to the upper limit of [Z/H] < 0.22 built in their models, which does not allow their metallicity profiles to go as high as ours in the centre of galaxies. In agreement with our findings, these authors also identify a clear σ–metallicity relation and a trend for metallicity gradient to get flatter at larger σ (primarily) and larger M_*. These trends are also confirmed by the detailed elemental abundance analysis by Parikh et al. ([2019](#)), based on a sample of 366 ETGs in MaNGA with a pure index fitting approach. The analysis of 303 MaNGA ellipticals by Domínguez Sánchez et al. ([2019](#)), where the IMF was allowed to vary among and within galaxies, also confirms steep metallicity gradients for the most massive and high-velocity-dispersion galaxies.

Different analyses of stellar populations across the galaxy extent have been published for the CALIFA survey as well. González Delgado et al. ([2015](#)) show the average radial profiles of mass-weighted log Z_* (as well as light-weighted log Age) for 41 Es and 32 S0s. Concerning the metallicity, they find remarkably flat profiles, with logarithmic slopes within 1 R_e of ~ 0 for the ellipticals and $\lesssim 0.1$ for the S0s (as inferred from their fig. 17). This appears inconsistent with the majority of the analysis published in the literature, although the reason for this is not obvious. In fact, using a largely overlapping observational data set, we find much steeper gradients.[5] Also Martín-Navarro et al. ([2018](#)) performed an analysis of SSP-equivalent age and metallicity profiles based on stellar absorption indices only, on a similar and largely overlapping CALIFA data set, and found relatively steep logarithmic slopes for the metallicity, in the range $\sim -0.25 – \sim -0.15$, hence much closer to our estimates and the rest of the literature.

This brief review on radial profiles of stellar metallicity in ETGs can be summarized as follows: *there is a general although not unanimous consensus on relatively steep metallicity gradients, with [$Z_*/Z_\odot$] values that are definitely supersolar in the centre and decrease to sub-solar values already at 1 R_e. Different results appear to be driven more by different modelling techniques rather than by the different observational data sets or statistical limitations.*

8.1.2 Local $\mu_* - Z_*$ relation

Most works in the literature focus on the dependence of metallicity on radius, yet we have shown that a very tight and quasi-universal relation is established between the local surface mass density in stars and their metallicity, whereby this relation is only modulated by σ_e (and by M_*) in second approximation. In a previous work González Delgado et al. ([2014](#)) have analysed a sample of 300 CALIFA galaxies covering the full range of morphology and stellar mass and concluded that both total stellar mass and local stellar mass density affect metallicity. In particular, they claim that in spheroids the main driver in changing metallicity is global (M_*), while local effects (μ_*) just modulate the global trends. Despite the direction of the trends being the same as ours, the importance of global-versus-local drivers is reversed. This is probably a consequence of their metallicity profiles in ETGs being much flatter than ours, a feature that is in contrast with large part of the previous literature.

On the other hand, it is interesting to note that Scott et al. ([2009](#)) showed a significant relation between local metallicity and the local escape velocity v_{esc} in SAURON galaxies, which becomes even tighter if a combination of age and metallicity is considered. However, this is only partially in agreement with our findings. In fact, these authors show that a tight relation between v_{esc} and μ_* exists *in each individual galaxy*, and this implies, in turn, a strong $\mu_* - Z_*$ relation. However, their relation between v_{esc} and μ_* shifts significantly as a function of galaxy mass. Therefore their analysis would not reproduce a universal $\mu_* - Z_*$ relation like the one we observe.

Finally, we point out that a significant correlation between surface density of dynamical mass and local Z_* was found by Zhuang

---

[5]Note that the averaging in González Delgado et al. ([2015](#)) is done on logarithmic quantities, whereas in this work we average the linear quantities. This may possibly lead to a relative negative bias with respect to our estimates and other works in literature (see also Appendix B, available online). Another possible cause of relative bias may be that STARLIGHT's best-fitting solutions are mostly determined by the overall shape of the SED (colours) and are somewhat biased towards larger ages, while other solutions of similar likelihood along the age–metallicity degeneracy curve are discarded.

et al. (2019) for a general sample of 244 CALIFA galaxies of all Hubble types, not only ETGs. Despite the stellar metallicity being derived with the same method as in this work, the results by Zhuang et al. (2019) strengthen the significance of our findings by using an independent estimate of mass surface density, solely based on dynamics, and by extending the relation to all morphologies.

8.1.3 Age profiles

Age profiles and gradients have been concurrently investigated with metallicity profiles in most of the works cited in the previous paragraphs. In general ETGs are found to have relatively flat age profiles, with overall variations within ~ 0.1 dex (25 per cent) inside $1\,R_e$. However, there is a broad diversity of results from different studies.

The strongest negative age gradients are reported by González Delgado et al. (2015, CALIFA), who found that the typical age decrease from ~ 10 Gyr in the centre to ~ 5 Gyr at $1\,R_e$, with a logarithmic slope of ~-0.3. Li et al. (2018, MaNGA) report age gradients broadly distributed around ~-0.08, with a significant number of galaxies displaying positive gradients. Similarly, Parikh et al. (2019) find mildly negative age gradients in their analysis of MaNGA ETGs. Typically flat profiles are reported by both Koleva et al. (2011) and Martín-Navarro et al. (2018, CALIFA). Interestingly, Goddard et al. (2017) show that light-weighted and mass-weighted ages have opposite gradients in their analysis of MaNGA ETGs: while the light-weighted age mildly decreases with radius, the mass-weighted age, which is overall larger by some 0.2 – 0.3 dex, increases with radius. This could be interpreted if we make the hypothesis that the SFH of the integrated (*in-situ* plus accreted) stellar population in the outer parts had a peak further in the past but a longer extension to recent times, with respect to the stellar populations in the inner parts. In yet another analysis of the MaNGA data, based on spectral indices, Domínguez Sánchez et al. (2019) report positive age gradients, but only for the most luminous ETGs ($-22.5 < M_r[\mathrm{mag}] < -23.5$) with the highest velocity dispersion ($2.40 < \log(\sigma_0/\mathrm{km\,s^{-1}}) < 2.50$), while negative age gradients are reported in all other bins. Finally, Kuntschner et al. (2010, SAURON) report mildly positive age gradients, with typical logarithmic slopes $\sim+0.05$ to $+0.1$. Similar values can be inferred from the aperture-integrated ages reported by McDermid et al. (2015, ATLAS$^{3\mathrm{D}}$).

Positive age gradients have been reported for S0 galaxies by different authors, based either on absorption features (e.g. Fisher, Franx & Illingworth 1996; Bedregal et al. 2011; Sil'chenko et al. 2012) or optical-NIR colours (Prochaska Chamberlain et al. 2011). They are typically interpreted as evidence of outside-in quenching.

Our U-shaped age profiles fall within the broad range of profile shapes and gradients that are reported in the literature. Assuming that the U-shape we measure is the true one, this may help explain part of the diversity of previous results, whereby a single constant logarithmic slope is assumed to describe a profile whose gradient changes its sign along the radius. However, this is (or may be) only part of the story: the different methods adopted in the different studies are certainly affected by different relative systematic biases, which stem, e.g. from the different population synthesis models, assumed SFH and metal distributions, observational constraints, and also different spatial resolution. These biases can easily exceed 0.1 dex and change in different regimes of age/metallicity.

We stress, on the other hand, that we rely on a very extended yet clean set of observables, i.e. indices that do not suffer of flux calibration issues and are chosen to be as insensitive as possible to ingredients that we can poorly model (e.g. variable elemental abundance ratios), plus photometry from 3500 to 9000 Å. Moreover, the spectral library we adopt for the interpretation allows for the broadest ignorance on the true SFH, chemical composition, and dust attenuation. Although, due to the complex pattern of mutual degeneracies, making a direct connection between the radial profiles of observed quantities and inferred physical parameters (age) is all but straightforward, in Appendix E (available online) we show that indeed the inflection of the age profiles corresponds to different changes of slopes in the colour and index profiles, which reassures us about the reality of the U-shape. Moreover, the fact that the amplitude of the age minimum correlates with a formally completely independent physical parameter such as σ_e is a strong indication that there is a real underlying physical effect. All this, together with the extensive testing we performed (see Section 3), makes us confident in the robustness of our results on the U-shape of the age profiles.

8.2 Which evolutionary scenario for ETGs?

From the theoretical point of view, spatial variations of stellar population properties are a key benchmark for our understanding of the formation and evolution of ETGs. Although the historical antithesis between the dissipative ('monolithic') collapse scenario and the naïve rendition of the hierarchical merging scenario, whereby an elliptical is the result of a spiral–spiral merger, is superseded by a much more complex picture where the typical physical mechanisms at work in both of them are deeply interlaced, these two pictures can still be seen as extreme or archetypical scenarios, which can apply to different phases and dominate in different galaxy regions.

Dissipative collapse models that do not implement any other feedback than stellar winds result in steep metallicity gradients with logarithmic slopes of ~-0.3 (e.g. Kobayashi 2004) and in positive age gradients as consequence of the outside-in quenching driven by stellar winds (so-called 'outside-in formation scenario', e.g. Pipino, D'Ercole & Matteucci 2008; Pipino et al. 2010).[6] Comparing these predictions with our results, we see that this can be only part of the story. While our observed metallicity gradients match the dissipative collapse predictions within $1\,R_e$, positive age gradients occur only at $R \gtrsim 0.4\,R_e$ and flatten out at $R \gtrsim 1\,R_e$. On the other hand, the effect of major mergers is to flatten the gradients significantly (e.g. Hopkins et al. 2009; Taylor & Kobayashi 2017) and to produce a large scatter. Therefore the observed steep metallicity gradients, ubiquitous in our sample, and the very small galaxy-to-galaxy scatter rule out the possibility that (the inner parts of) ETGs are heavily affected by recent major mergers.

One possible way to explain the observed reversal of the age gradients inside $\sim 0.4\,R_e$ (hence the presence of an age minimum) is to invoke some mechanism of *quenching that acts from the inside outwards*. Such an inside-out quenching is indeed observed in massive star-forming galaxies at $z \sim 2$ (e.g. Tacchella et al. 2015, 2018). *Dynamical heating* due to the growing stellar density ('morphological quenching', e.g. Martig et al. 2009) or *AGN feedback* could both represent plausible physical mechanisms to shut down star-formation progressively from the nucleus outwards. This would

---

[6]Note that a similar effect of outside-in quenching may be produced also by AGN feedback, as recent simulations by Brennan et al. (2018) indicate.

also qualitatively fit the observation that the age minimum is deeper for lower-σ_e galaxies. In fact, in the case of AGN feedback, given the relation that exists between the mass of the central supermassive black hole and the velocity dispersion of galaxies (e.g. Gebhardt et al. 2000), we can envisage that galaxies with higher σ_e had a more powerful and effective AGN, that was able to shut down the star formation more quickly and up to larger radii, while lower-σ_e galaxies were able to proceed in their outside-in dissipative-like formation for longer time. In fact, we do observe that the age profiles of the lowest-σ_e ETGs in our sample approach a radially almost-monotonic increasing behaviour. This scenario needs more testing, especially in a quantitative sense, to be confirmed. High-resolution simulations are being analysed by our group and results will be presented in a future paper (Hirschmann et al., in preparation).

Alternatively, the shapes of the age profiles may be qualitatively explained by a scenario in which ETGs form the bulk of their stars within $\sim 1 R_e$ on time-scales that would result in negligible age gradients as observed today. On the top of these stars, more recent gas accretion may produce episode(s) of the so-called '*disc re-growth*', which rejuvenates the stellar population (De Lucia et al. 2011). Such a process, however, would have a variable intensity as a function of radius and, in particular, the conversion of gas into stars may be prevented by the hot dynamical state in the inner regions. This would produce a minimum in the age profiles at intermediate radii as a sort of fossil record of such episodes. The dependence of the age gradient inversion on the velocity dispersion is also in qualitative agreement with this hypothesis, in that ETGs with higher velocity dispersion appear less affected by this kind of rejuvenation than ETGs with lower σ_e. Although plausible, also this second scenario is purely speculative at this stage, and more testing (e.g. by checking against stellar kinematics) and simulations are needed.

Finally, the flattening of the gradients, both in age and metallicity, beyond $\sim 1.5 R_e$, can be interpreted as the transition to a regime, which develops in a *second phase* of galaxy formation, where *stars accreted from satellites* start to represent a portion comparable to the one provided by the *in-situ* formed stars, according to simulations (see e.g. Hirschmann et al. 2015; Rodriguez-Gomez et al. 2016). Specifically, the lower mass of the accreted satellites would explain why the metallicity profiles flatten out to sub-solar values $\log Z_*/Z_\odot \sim -0.1$ (see also Oyarzún et al. 2019). The accreted satellites would have been quenched early on (see Pasquali et al. 2010, 2019), and this would explain why the age profiles flatten out to maximally old ages of ≈ 10 Gyr. Support to such a second phase of ex-situ stellar accretion is also lent by observations of the distinct chemical and kinematic properties of the stars at large radii (see e.g. Coccato, Gerhard & Arnaboldi 2010; Pulsoni et al. 2018).

This *two-phase formation scenario* for ETGs resembles very closely the one proposed by Oser et al. (2010), purely based on cosmological simulations (see also e.g. De Lucia et al. 2006; Navarro-González et al. 2013). Moreover, it provides a natural explanation for the evolution of high-redshift compact passive galaxies, which are commonly interpreted as the descendants of compact sub-mm galaxies that quickly formed stars in an intense dissipative episode and then grow to present-day ETGs via minor mergers (e.g. see Oser et al. 2012; Toft et al. 2014; Choi et al. 2018). In this framework it is also possible to explain, at least qualitatively, many of the open issues that we outlined in the Introduction. Chiefly this applies to the size growth, but also the enhancement in α elements and the systematic variations of IMF may be interpreted as a consequence of the different density at which stars belonging

to different (portions of) galaxies were formed, either in the main progenitor(s) or in the accreted satellites.

9 SUMMARY AND CONCLUSIONS

In this paper we have analysed the spatial variations of the *r*-band-light-weighted mean age and metallicity of the stellar populations in 69 ETGs drawn from the CALIFA survey, including 48 ellipticals and 21 S0s. Our analysis is based on a Bayesian statistical approach, whereby a state-of-the-art suite of 500 000 spectral synthesis models is compared to the observed maps of stellar absorption indices and broad-band fluxes, which is so far unique in the literature. The large field of view and the depth of the CALIFA-SDSS data set is such that we can reliably cover the radial extent of our galaxies out to $1.5 R_e$ ($2 R_e$) for 74 per cent (46 per cent) of the sample with a median resolution of $0.08 R_e$, and we are essentially complete to stellar mass surface density of $100 M_\odot$ pc^{-2}.

We have shown that steep negative radial gradients in metallicity are ubiquitous and very consistent among galaxies over a relatively broad range of velocity dispersion, stellar mass, and morphology. The central regions of ETGs reach metallicities more than twice solar and decrease below solar abundance between 1 and $1.5 R_e$. On the contrary, age profiles show relatively small radial variations, of the order of 40 per cent at most on average. The most striking feature of the age profiles is that, on average, there is an inversion of slope at $\sim 0.3 - 0.4 R_e$, where a minimum age is reached, i.e. profiles are U-shaped. All ETGs share maximally old ages at large galactocentric distances (SMA $\gtrsim 1.5 R_e$). Within $\sim 1 R_e$ we note an increased scatter, that mainly correlates with the global velocity dispersion of the galaxies, σ_e. High-σ_e galaxies display a shallow minimum at $\sim 0.3 - 0.4 R_e$ and older age in the centre. For lower-σ_e galaxies the minimum age decreases and the inversion of the age profile towards the centre becomes weaker.

Metallicity appears to be primarily determined by the local stellar mass surface density μ_*, as shown by the tiny galaxy-to-galaxy scatter in the Z_* versus μ_* plot. There is, in fact, a *quasi-universal local mass–metallicity relation*, which is only mildly modulated by σ_e, whereby the highest-σ_e galaxies (~ 300 km s^{-1}) have their metallicity profiles offset to ~ 0.15 dex higher values than the lowest-σ_e ones (~ 150 km s^{-1}). This result confirms in greater detail, yet over a more limited set of galaxies, the findings by Zhuang et al. (2019).

For both age and metallicity, we have analysed in great detail possible dependencies of profile shapes, normalizations, and gradients on global galaxy properties, such as σ_e, stellar mass, morphology, light-concentration, global age, and metallicity. We showed that the most significant correlations are found with σ_e. Correlations with stellar mass are weaker and appear as largely inherited from the correlations with σ_e via the σ_e–mass relation. All other parameters, including morphology (i.e. E versus S0), affect the profiles only in a minor way, if anything.

Finally, we have discussed how the observations reported in this work support a two-phase formation scenario for ETGs. The first phase would be dominated by *in-situ* star formation in a dissipative collapse (series of) episode(s), which determines the (inner) strongly negative metallicity gradient and, due to outside-in wind-driven quenching, an initial positive age gradient. The onset of powerful AGN feedback (whose effectiveness scales with σ_e, via the well-known correlation between this quantity and the mass of the central black hole) or the development of strong dynamical heating would determine an inside-out quenching, hence the reversal in the age

profiles that we observe at $0.3 - 0.4\,R_e$. Alternatively, the age minimum at $\sim 0.4 R_e$ might be the fossil record of disc regrowth in the inner regions, whose star formation efficiency is regulated (or suppressed) by the local velocity dispersion. This phase would be mainly recorded in the properties of the inner $\sim 1\,R_e$. Outside of this radius, a second phase dominated by minor mergers and accretion events of early-on quenched satellites would then produce the flattening of the profiles around ages of $\sim 10\,\mathrm{Gyr}$ and sub-solar metallicities.

In a forthcoming paper (Hirschmann et al., in preparation) we will investigate how cosmological SPH simulations at high-resolution and implementing AGN feedback can reproduce the current observations and possibly lend support to the proposed scenario.

REFERENCES

Abazajian K. N. et al., 2009, ApJS, 182, 543
Barrera-Ballesteros J. K. et al., 2016, MNRAS, 463, 2513
Bedregal A. G., Cardiel N., Aragón-Salamanca A., Merrifield M. R., 2011, MNRAS, 415, 2063
Bender R., Burstein D., Faber S. M., 1993, ApJ, 411, 153
Brennan R., Choi E., Somerville R. S., Hirschmann M., Naab T., Ostriker J. P., 2018, ApJ, 860, 14
Brough S., Proctor R., Forbes D. A., Couch W. J., Collins C. A., Burke D. J., Mann R. G., 2007, MNRAS, 378, 1507
Bruzual G., Charlot S., 2003, MNRAS, 344, 1000
Bryant J. J. et al., 2015, MNRAS, 447, 2857
Bundy K. et al., 2015, ApJ, 798, 7
Cano-Díaz M. et al., 2016, ApJ, 821, L26
Cappellari M., Emsellem E., 2004, PASP, 116, 138
Cappellari M. et al., 2011, MNRAS, 413, 813
Carollo C. M., Danziger I. J., Buson L., 1993, MNRAS, 265, 553
Chabrier G., 2003, ApJ, 586, L133
Charlot S., Fall S. M., 2000, ApJ, 539, 718
Choi E., Somerville R. S., Ostriker J. P., Naab T., Hirschmann M., 2018, ApJ, 866, 91
Coccato L., Gerhard O., Arnaboldi M., 2010, MNRAS, 407, L26
Conroy C., van Dokkum P. G., 2012, ApJ, 760, 71
Consolandi G., Gavazzi G., Fumagalli M., Dotti M., Fossati M., 2016, A&A, 591, A38
Croton D. J. et al., 2006, MNRAS, 365, 11
D'Souza R., Bell E. F., 2018, MNRAS, 474, 5300
da Cunha E., Charlot S., Elbaz D., 2008, MNRAS, 388, 1595
De Lucia G., Springel V., White S. D. M., Croton D., Kauffmann G., 2006, MNRAS, 366, 499
De Lucia G., Fontanot F., Wilman D., Monaco P., 2011, MNRAS, 414, 1439
de Vaucouleurs G., 1948, Ann. Astrophys., 11, 247
de Vaucouleurs G., 1961, ApJS, 5, 233
de Vaucouleurs G., de Vaucouleurs A., Corwin H. G. Jr, Buta R. J., Paturel G., Fouque P., 1991, Third Reference Catalogue of Bright Galaxies. Volume 1-3, XII, 2069. Springer-Verlag Berlin Heidelberg, New York, p. 7
de Zeeuw P. T. et al., 2002, MNRAS, 329, 513
Domínguez Sánchez H., Bernardi M., Brownstein J. R., Drory N., Sheth R. K., 2019, MNRAS, 489, 5612
Eggen O. J., Lynden-Bell D., Sandage A. R., 1962, ApJ, 136, 748
Emsellem E. et al., 2011, MNRAS, 414, 888
Falcón-Barroso J., Sánchez-Blázquez P., Vazdekis A., Ricciardelli E., Cardiel N., Cenarro A. J., Gorgas J., Peletier R. F., 2011, A&A, 532, A95
Falcón-Barroso J., Lyubenova M., van de Ven G., 2015, in Cappellari M., Courteau S., eds, Proc. IAU Symp. Vol. 311, Galaxy Masses as Constraints of Formation Models. University of Oxford, Oxford, UK, p. 78
Falcón-Barroso J. et al., 2017, A&A, 597, A48
Ferreras I., La Barbera F., de La Rosa I. G., Vazdekis A., de Carvalho R. R., Falcon-Barroso J., Ricciardelli E., 2013, MNRAS, 429, L15
Fisher D., Franx M., Illingworth G., 1996, ApJ, 459, 110
Gallazzi A., Charlot S., Brinchmann J., White S. D. M., Tremonti C. A., 2005, MNRAS, 362, 41
Gallazzi A., Charlot S., Brinchmann J., White S. D. M., 2006, MNRAS, 370, 1106
Gavazzi G., Scodeggio M., 1996, A&A, 312, L29
Gebhardt K. et al., 2000, ApJ, 539, L13
Goddard D. et al., 2017, MNRAS, 466, 4731
González Delgado R. M. et al., 2014, ApJ, 791, L16
González Delgado R. M. et al., 2015, A&A, 581, A103
González Delgado R. M. et al., 2016, A&A, 590, A44
Hirschmann M., Naab T., Ostriker J. P., Forbes D. A., Duc P.-A., Davé R., Oser L., Karabal E., 2015, MNRAS, 449, 528
Hopkins P. F., Cox T. J., Dutta S. N., Hernquist L., Kormendy J., Lauer T. R., 2009, ApJS, 181, 135
Ibarra-Medel H. J., Avila-Reese V., Sánchez S. F., González-Samaniego A., Rodríguez-Puebla A., 2019, MNRAS, 483, 4525
Kauffmann G. et al., 2003, MNRAS, 341, 54
Kelz A. et al., 2006, PASP, 118, 129
Kobayashi C., 2004, MNRAS, 347, 740
Koleva M., Prugniel P., De Rijcke S., Zeilinger W. W., 2011, MNRAS, 417, 1643
Kuntschner H. et al., 2010, MNRAS, 408, 97
Larson R. B., 1974, MNRAS, 166, 585
Li H. et al., 2018, MNRAS, 476, 1765
Marigo P., Bressan A., Nanni A., Girardi L., Pumo M. L., 2013, MNRAS, 434, 488
Martig M., Bournaud F., Teyssier R., Dekel A., 2009, ApJ, 707, 250
Martín-Navarro I., La Barbera F., Vazdekis A., Falcón-Barroso J., Ferreras I., 2015, MNRAS, 447, 1033
Martín-Navarro I., Vazdekis A., Falcón-Barroso J., La Barbera F., Yıldırım A., van de Ven G., 2018, MNRAS, 475, 3700
McDermid R. M. et al., 2015, MNRAS, 448, 3484
Mehlert D., Thomas D., Saglia R. P., Bender R., Wegner G., 2003, A&A, 407, 423
Navarro-González J., Ricciardelli E., Quilis V., Vazdekis A., 2013, MNRAS, 436, 3507
Neistein E., van den Bosch F. C., Dekel A., 2006, MNRAS, 372, 933

Oser L., Ostriker J. P., Naab T., Johansson P. H., Burkert A., 2010, ApJ, 725, 2312

Oser L., Naab T., Ostriker J. P., Johansson P. H., 2012, ApJ, 744, 63

Oyarzún G. A. et al., 2019, ApJ, 880, 111

Parikh T. et al., 2019, MNRAS, 483, 3420

Pasquali A., Gallazzi A., Fontanot F., van den Bosch F. C., De Lucia G., Mo H. J., Yang X., 2010, MNRAS, 407, 937

Pasquali A., Smith R., Gallazzi A., De Lucia G., Zibetti S., Hirschmann M., Yi S. K., 2019, MNRAS, 484, 1702

Pipino A., D'Ercole A., Matteucci F., 2008, A&A, 484, 679

Pipino A., D'Ercole A., Chiappini C., Matteucci F., 2010, MNRAS, 407, 1347

Prochaska Chamberlain L. C., Courteau S., McDonald M., Rose J. A., 2011, MNRAS, 412, 423

Pulsoni C. et al., 2018, A&A, 618, A94

Reda F. M., Proctor R. N., Forbes D. A., Hau G. K. T., Larsen S. S., 2007, MNRAS, 377, 1772

Renzini A., 2006, ARA&A, 44, 141

Rodriguez-Gomez V. et al., 2016, MNRAS, 458, 2371

Roth M. M. et al., 2005, PASP, 117, 620

Sánchez-Blázquez P. et al., 2006, MNRAS, 371, 703

Sánchez-Blázquez P., Forbes D. A., Strader J., Brodie J., Proctor R., 2007, MNRAS, 377, 759

Sánchez S. F. et al., 2012, A&A, 538, A8

Sánchez S. F. et al., 2016, A&A, 594, A36

Sandage A., 1986, A&A, 161, 89

Sarzi M. et al., 2006, MNRAS, 366, 1151

Scodeggio M., Gavazzi G., Franzetti P., Boselli A., Zibetti S., Pierini D., 2002, A&A, 384, 812

Scott N. et al., 2009, MNRAS, 398, 1835

Sil'chenko O. K., Proshina I. S., Shulga A. P., Koposov S. E., 2012, MNRAS, 427, 790

Smith M. W. L. et al., 2012, ApJ, 756, 40

Spolaor M., Proctor R. N., Forbes D. A., Couch W. J., 2009, ApJ, 691, L138

Tacchella S. et al., 2015, Science, 348, 314

Tacchella S. et al., 2018, ApJ, 859, 56

Taylor P., Kobayashi C., 2017, MNRAS, 471, 3856

Toft S. et al., 2014, ApJ, 782, 68

Trager S. C., Faber S. M., Worthey G., González J. J., 2000, AJ, 120, 165

van der Wel A. et al., 2014, ApJ, 788, 28

Verheijen M. A. W., Bershady M. A., Andersen D. R., Swaters R. A., Westfall K., Kelz A., Roth M. M., 2004, Astron. Nachr., 325, 151

Walcher C. J. et al., 2014, A&A, 569, A1

Zhuang Y., Leaman R., van de Ven G., Zibetti S., Gallazzi A., Zhu L., Falcón-Barroso J., Lyubenova M., 2019, MNRAS, 483, 1862

Zibetti S., 2009, preprint (arXiv:0911.4956)

Zibetti S., Charlot S., Rix H.-W., 2009, MNRAS, 400, 1181

Zibetti S. et al., 2017, MNRAS, 468, 1902

SUPPORTING INFORMATION

Supplementary data are available at *MNRAS* online.

ONLINE APPENDICES

Please note: Oxford University Press is not responsible for the content or functionality of any supporting materials supplied by the authors. Any queries (other than missing material) should be directed to the corresponding author for the article.

This paper has been typeset from a TeX/LaTeX file prepared by the author.